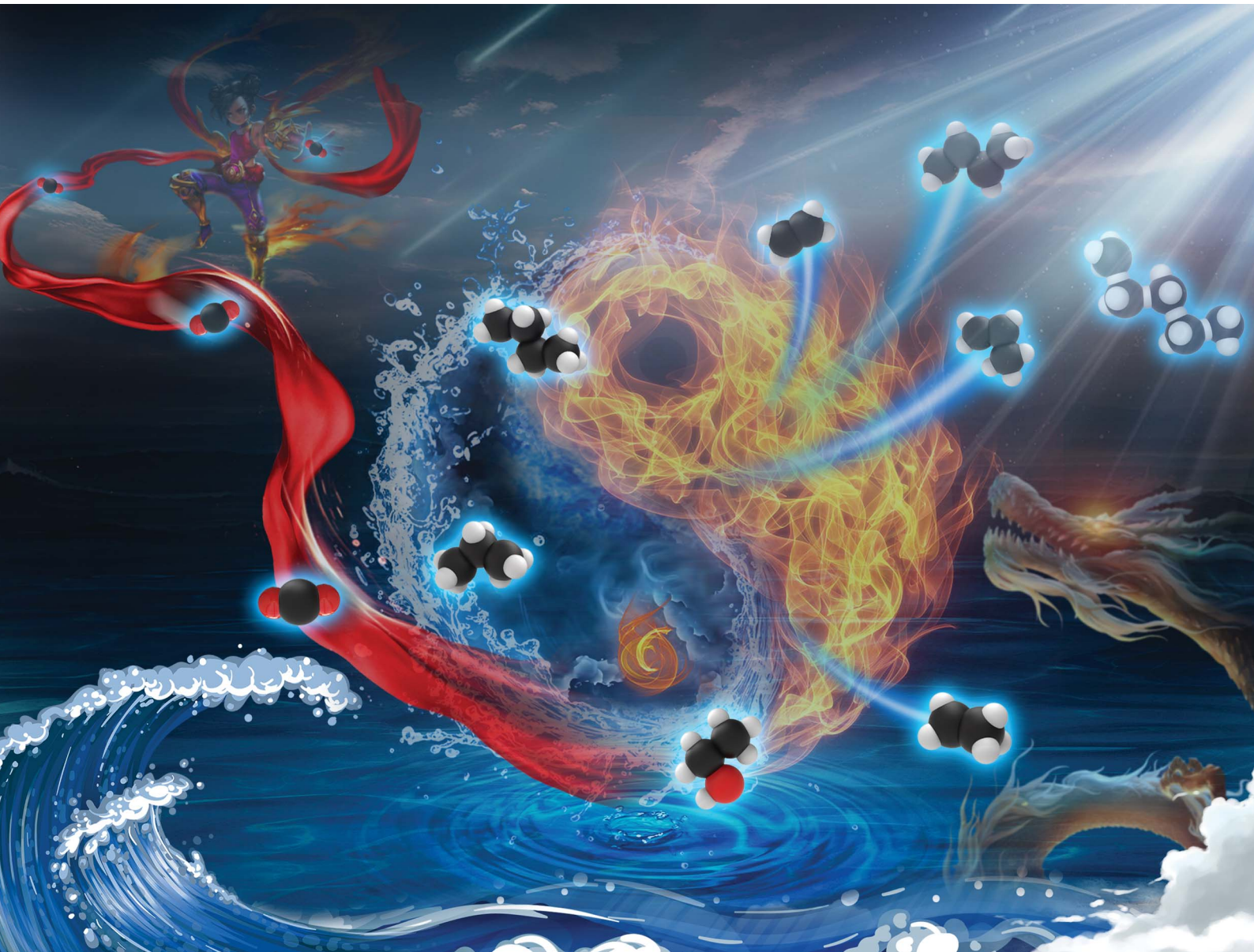


# Chemical Science

[rsc.li/chemical-science](https://rsc.li/chemical-science)



ISSN 2041-6539

REVIEW ARTICLE

Shangbo Ning, Jing Wang, Jinhua Ye *et al.*  
Recent advances and developments in solar-driven  
photothermal catalytic  $\text{CO}_2$  reduction into multicarbon ( $\text{C}_{2+}$ )  
products

## REVIEW

[View Article Online](#)  
[View Journal](#) | [View Issue](#)



Cite this: *Chem. Sci.*, 2025, **16**, 4568

## Recent advances and developments in solar-driven photothermal catalytic $\text{CO}_2$ reduction into multicarbon ( $\text{C}_{2+}$ ) products

Xiuting Wu,<sup>†,ab</sup> Senlin Zhang,<sup>†,a</sup> Shangbo Ning, <sup>\*a</sup> Chuanyun Yang,<sup>a</sup> Ling Li,<sup>a</sup> Linjun Tang,<sup>a</sup> Jing Wang,<sup>\*,b</sup> Ruixiang Liu,<sup>a</sup> Xingyu Yin,<sup>a</sup> Ying Zhu,<sup>a</sup> Shaohua Chen<sup>a</sup> and Jinhua Ye <sup>\*acd</sup>

Solar-driven catalytic conversion of carbon dioxide ( $\text{CO}_2$ ) into value-added  $\text{C}_{2+}$  chemicals and fuels has attracted significant attention over the past decades, propelled by urgent environmental and energy demands. However, the catalytic reduction of  $\text{CO}_2$  continues to face significant challenges due to inherently slow reduction kinetics. This review traces the historical development and current state of photothermal  $\text{CO}_2$  reduction, detailing the mechanisms by which  $\text{CO}_2$  is transformed into  $\text{C}_{2+}$  products. A key focus is on catalyst design, emphasizing surface defect engineering, bifunctional active site and co-catalyst coupling to enhance the efficiency and selectivity of solar-driven  $\text{C}_{2+}$  synthesis. Key reaction pathways to both  $\text{C}_1$  and  $\text{C}_{2+}$  products are discussed, ranging from  $\text{CO}$ ,  $\text{CH}_4$  and methanol ( $\text{CH}_3\text{OH}$ ) synthesis to the production of  $\text{C}_{2-4}$  products such as  $\text{C}_{2-4}$  hydrocarbons, ethanol, acetic acid, and various carbonates. Notably, the advanced synthesis of  $\text{C}_{5+}$  hydrocarbons exemplifies the remarkable potential of photothermal technologies to effectively upgrade  $\text{CO}_2$ -derived products, thereby delivering sustainable liquid fuels. This review provides a comprehensive overview of fundamental mechanisms, recent breakthroughs, and pathway optimizations, culminating in valuable insights for future research and industrial-scale prospect of photothermal  $\text{CO}_2$  reduction.

Received 14th January 2025  
Accepted 13th February 2025

DOI: 10.1039/d5sc00330j  
[rsc.li/chemical-science](http://rsc.li/chemical-science)

<sup>a</sup>Research Center for Solar Driven Carbon Neutrality, The College of Physics Science and Technology, Hebei University, Baoding 071002, China. E-mail: ningshangbo@hbu.edu.cn; jinhua.ye@hbu.edu.cn

<sup>b</sup>Key Laboratory of Analytical Science and Technology of Hebei Province, College of Chemistry and Materials Science, Hebei University, Baoding, 071002, China. E-mail: wangjing9804@163.com

<sup>c</sup>International Center for Materials Nanoarchitectonics (WPI-MANA), National Institute for Materials Science (NIMS), Tsukuba 305-0047, Japan. E-mail: jinhua.YE@nims.go.jp

<sup>d</sup>Advanced Catalytic Materials Research Center, School of Material Science and Engineering, Tianjin University, Tianjin 300072, China

† These authors contributed equally to this work.



Shangbo Ning

Dr Shangbo Ning is associate professor of materials science and optical engineering in Hebei University, China and member of the Research Center for the Solar Driven Carbon Neutrality. He received his PhD degree from the Tianjin University under the supervision of professor Jinhua Ye and engaged in postdoctoral research at the China University of Mining and Technology from 2023 to 2025. His research interests focus on the research

and development of novel photocatalytic materials and their applications in the fields of energy and environment photo-/photothermal-catalysis and solar to chemical energy conversion.



Jing Wang

Dr Jing Wang received her PhD from Huazhong University of Science and Technology (2009–2013) and was a visiting scholar at Georgia State University (2016). She is a professor and master's supervisor, recognized with the inaugural China Youth Science and Technology Innovation Award. She has published over 100 SCI papers, holds multiple patents, and has led national and provincial research projects. A recipient of several scientific awards, she was listed among the world's top 2% scientists in 2020.



## 1. Introduction

The escalating impact of climate change and environmental degradation, primarily attributed to the widespread use of fossil fuels, highlights the necessity for effective approaches to curb.<sup>1,2</sup> As the principal greenhouse gas, CO<sub>2</sub> not only poses severe environmental threats but also presents a potential carbon feedstock for synthesizing high-value chemicals and fuels.<sup>3–7</sup> Compared with C<sub>1</sub> products such as CH<sub>4</sub> and CO, multicarbon (C<sub>2+</sub>) hydrocarbon products not only have higher energy density, but also are convenient for transportation and storage, which is of great significance in the field of CO<sub>2</sub> reduction.<sup>8</sup> However, the thermodynamic and kinetic stability of CO<sub>2</sub> renders its catalytic transformation into C<sub>2+</sub> products particularly challenging, thereby requiring novel approaches capable of breaking the linear trade-off between high selectivity and high conversion.

Photothermal catalysis has emerged as a promising avenue for transforming CO<sub>2</sub> into valuable C<sub>2+</sub> products by harnessing the dual benefits of solar irradiation and thermal energy.<sup>8–10</sup> In contrast to purely thermal routes, photothermal catalysis leverages both the photonic energy (often manifested through photoexcited charge carriers in semiconductor or plasmonic materials) and the thermal energy generated from converting unabsorbed light (especially in the infrared region) into heat.<sup>11</sup> This synergy offers the potential to accelerate reaction kinetics at relatively lower overall temperatures and to enhance reaction selectivity by modulating critical steps such as CO<sub>2</sub> adsorption, intermediate formation (e.g. \*CO, formate), and C–C coupling.<sup>12–14</sup> Directing the reaction pathway toward C<sub>2+</sub> products calls for rational control of active sites, defect engineering, and local reaction environments, which can be made possible through an integrated photothermal approach.

Despite these advantages, achieving efficient and scalable photothermal CO<sub>2</sub> reduction to C<sub>2+</sub> products remains

challenging. Catalysts must be meticulously engineered at multiple levels, encompassing nanoscale morphology, surface functionalization, and the precise tuning of electronic structures to activate and stabilize multi-carbon intermediates. Equally critical is the design of reactors to ensure optimal photon capture, uniform heat distribution, and accurate control of the reaction atmosphere. Addressing these challenges will require synergistic advancements in catalyst development, reactor engineering, and process optimization, paving the way for the practical realization of photothermal CO<sub>2</sub> conversion technologies with high efficiency and scalability.

In this review, we focus on the rapid developments and emerging prospects for photothermal CO<sub>2</sub> reduction, emphasizing the formation of C<sub>2+</sub> products as a viable strategy for enhancing the economic and practical value of CO<sub>2</sub> utilization. After outlining the historical context and current imperatives of photothermal CO<sub>2</sub> reduction, we delve into the mechanistic insights that underpin the photothermal conversion of CO<sub>2</sub> to C<sub>2+</sub> products. We then discuss critical aspects of catalyst design, including surface defect engineering, bifunctional active site construction and co-catalyst coupling, which are instrumental in realizing efficient C<sub>2+</sub> production. Finally, we provide an overview of key solar-driven CO<sub>2</sub> reduction pathways, categorized according to product type, ranging from C<sub>1</sub> to C<sub>2+</sub> products. Furthermore, this review aims to highlight the pivotal role of C<sub>5+</sub> products in shaping the future of photothermal CO<sub>2</sub> upgrading, as these high-value hydrocarbons hold immense potential for sustainable fuel and chemical production. By addressing the challenges and identifying future directions, this review provides both theoretical and practical guidance for researchers and engineers striving to enhance the efficiency, selectivity, and scalability of C<sub>2+</sub> products synthesis, ultimately paving the way for large-scale, sustainable implementations in industrial applications.



Jinhua Ye

Professor Jinhua Ye received her PhD from the University of Tokyo in 1990, and joined National Research Institute for Metals (former organization of NIMS) in 1991. She is now the appointed director of Research Center for Solar Driven Carbon Neutrality, Hebei University, China. Her research interests focus on the research and development of photo functional materials and their applications in the fields of environment preservation and

new energy production. She has been admitted as a Fellow of the Royal Society of Chemistry since 2016, and also selected as 2016, 2018–2024 Highly Cited Researcher (Clarivate Analytics), 2022 Pioneer in Energy Research (ACS Publications). She is currently serving as the Associate Editor of ACS Nano, and Science Advances (AAAS).

### 1.1 History and reality of photothermal CO<sub>2</sub> reduction

Global population growth and rising living standards have led to increased energy consumption, with 85% of energy coming from fossil fuels, potentially causing an energy crisis and severe environmental challenges.<sup>15–19</sup> A prominent issue is global warming, caused by the emission of greenhouse gases like CO<sub>2</sub>, methane (CH<sub>4</sub>).<sup>16,20–24</sup>

Against the backdrop of escalating energy demands and environmental concerns, technologies for converting CO<sub>2</sub> have garnered significant attention. CO<sub>2</sub>, as an abundant carbon source, holds promise not only for mitigating greenhouse gas emissions but also for serving as a resource in the synthesis of valuable chemicals and fuels. In the early 20th century, as catalysis emerged as a scientific discipline, researchers discovered the effectiveness of metallic and metalloid catalysts in reducing CO<sub>2</sub>.<sup>25</sup> As shown in Fig. 1, in 1902, Paul Sabatier published seminal work, “New Synthesis of Methane”, documenting the catalytic conversion of H<sub>2</sub> and CO<sub>2</sub> into CH<sub>4</sub> and H<sub>2</sub>O using a Ni catalyst at elevated temperatures. This process became known as the Sabatier reaction.<sup>25</sup>



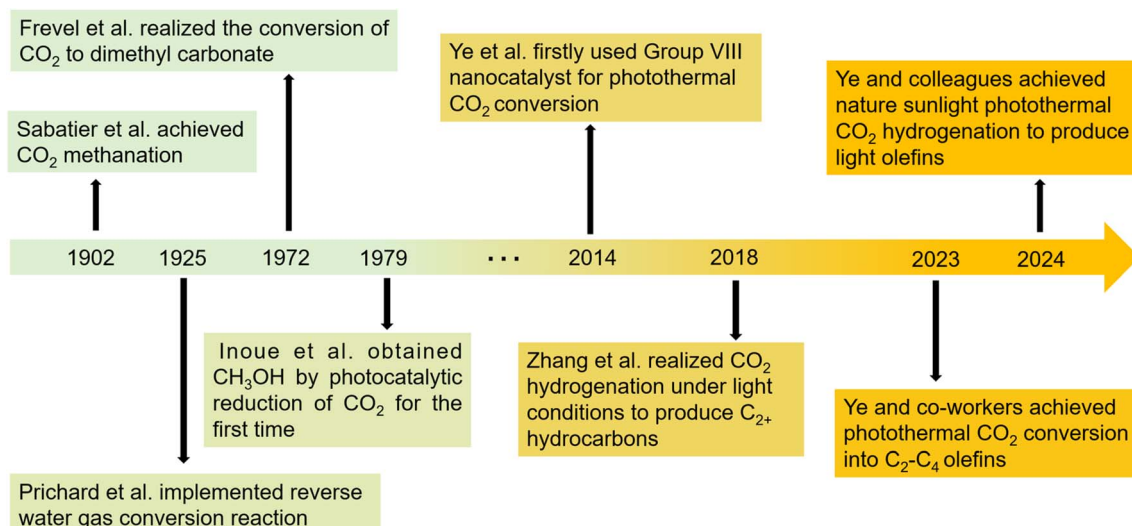


Fig. 1 The history and recent advances of catalytic conversion of  $\text{CO}_2$  into  $\text{C}_{2+}$  products.

The timeline of development continued until the late 1970s, highlighted by Fujishima and Honda's groundbreaking work in 1972, which laid the foundation for photocatalysis.<sup>26</sup> Since then, interest in heterogeneous photocatalysts for converting solar energy into chemical energy has surged.<sup>27-33</sup> Despite the development of various semiconductor photocatalysts, practical solar energy conversion efficiency has been unsatisfactory. This low efficiency is due to inadequate absorption of the solar spectrum, especially in the visible light and near-infrared (NIR) regions,<sup>34</sup> and the rapid recombination of photoexcited charge carriers.<sup>35,36</sup>

Entering the 1970s and 1980s, as photocatalytic technology was studied more deeply, researchers sought more efficient photocatalysts.  $\text{TiO}_2$  became a popular research focus due to its stability and cost-effectiveness.<sup>37</sup> Juraj Kizlink *et al.* reported using organotin(II) compounds to synthesize dimethyl carbonate from  $\text{CO}_2$  and  $\text{CH}_3\text{OH}$ .<sup>38</sup> Meanwhile, thermal catalysis also saw advancements with the development of various metal and metal oxide catalysts for  $\text{CO}_2$  reduction.<sup>39</sup> By the 1990s, research on photocatalysis and thermal catalysis mechanisms deepened, focusing on catalyst active sites and reaction pathways, providing a theoretical basis for catalyst design and optimization.<sup>40,41</sup>

Since the early 21st century, the research in photocatalysis and thermal catalysis has been optimized. In photocatalysis, researchers have refined reaction parameters like temperature, light intensity, and developed more efficient reactors.<sup>42</sup> In thermal catalysis, strategies like alloying, doping, and support modification have enhanced catalyst activity, selectivity, and stability.<sup>43</sup> In 2014, Ye's group firstly demonstrated the effective use of sunlight and superior photothermal properties of VIII metal-based nanocatalysts, highlighting their unique activation capability for  $\text{CO}_2$  hydrogenation.<sup>44</sup> Photothermal catalysis, a field that has gained considerable attention in recent years, is regarded as a promising avenue for maximizing the efficiency of solar energy utilization. This approach merges the benefits of

both thermal and photocatalytic processes, offering excellent catalytic performance even under mild conditions.<sup>45</sup> Rather than a mere combination, photothermal catalysis represents a synergistic interaction between photocatalysis and thermal catalysis.<sup>46-48</sup> The light can convert to heat, which initiates  $\text{CO}_2$  reduction reaction, while the photo-excited charge carriers can also regulate reactivity and product selectivity, with reaction efficiency being further enhanced by the heat produced during thermochemical reaction. It optimizes the use of solar energy for the efficient transformation of  $\text{CO}_2$ . The photothermal catalysis can reduce the activation energy required for  $\text{CO}_2$  conversion and fine-tune the reaction pathways by modulating the electronic structure of catalytic materials, thereby enhancing the selectivity of desired products.<sup>49</sup> In 2017, Zeng's team reported the  $\text{Au}\&\text{Pt}@\text{ZIF}$  catalyst, which combines photothermal effects with insulating properties, reducing the temperature needed for  $\text{CO}_2$  hydrogenation.<sup>50</sup> In particular, the development of efficient new catalysts has become a research hotspot for converting photothermally-driven  $\text{CO}_2$  into  $\text{C}_{2+}$  products.<sup>51</sup> For instance, in 2018, Zhang's group developed novel CoFe-based catalysts by reducing CoFeAl layered double hydroxide (LDH) nanosheets with hydrogen at 300–700 °C. These CoFe-x catalysts showed a shift in selectivity from CO to  $\text{CH}_4$  and then to  $\text{C}_{2+}$  under UV-visible light, with selectivity varying based on the reduction temperature of the LDH nanosheets.<sup>52</sup>

Our research group, dedicated to advancing photothermal  $\text{CO}_2$  conversion into  $\text{C}_{2+}$  products, has achieved significant progress. By altering the electronic structure, photoelectrons can enhance selectivity and prolong catalyst longevity.<sup>53</sup> Photothermal catalysis, which combines photocatalysis and thermal catalysis, is a rapidly advancing technology. It utilizes light to generate heat and excite electron–hole pairs, providing an innovative method for  $\text{CO}_2$  reduction.<sup>54</sup> We developed a photo-thermal synergistic catalytic system by integrating Co and Cu nanoparticles onto  $\text{SrTiO}_3$ , demonstrating enhanced



performance in Fischer-Tropsch synthesis.<sup>55</sup> Meanwhile, we introduced a bifunctional catalyst with  $\text{Co}^0\text{--Co}^{\delta+}$  active centers on  $\text{MgAl}_2\text{O}_4$  for photothermal-driven  $\text{CO}_2$  conversion into  $\text{C}_{2-4}$  olefins. These studies underscore the importance of carefully engineered metal/oxide interfaces for achieving selective  $\text{CO}_2$  hydrogenation into higher-value products, advancing both sustainable chemical processes and renewable energy utilization.<sup>9</sup> In addition, we synthesized a Cu-modified CoFe alloy catalyst *via* an enhanced sol-gel method for solar-driven  $\text{CO}_2$  hydrogenation, which effectively promotes  $\text{CO}_2$  adsorption and hydrogenation, leading to high selectivity toward  $\text{C}_{2+}$  hydrocarbons and  $\text{C}_{2-4}$  olefins.<sup>56</sup> Currently, photothermal-catalytic  $\text{CO}_2$  conversion predominantly yields  $\text{C}_{2-4}$  products, while  $\text{C}_{5+}$  products are still generated in relatively low quantities. There is a pressing need to develop more efficient catalysts and processes that can boost both the yield and selectivity of  $\text{C}_{5+}$  products.

Recent advances in this field underscore a sustained emphasis on solar-driven catalytic processes for  $\text{CO}_2$  conversion, which continues to be a focal area of research. Notably, the push toward producing higher-value  $\text{C}_{2+}$  hydrocarbons from  $\text{CO}_2$  has gained significant traction, highlighting the substantial promise and expanding prospects of  $\text{CO}_2$  high-added value conversion for sustainable energy applications. This progress demonstrates the potential of light-driven catalysis as a sustainable solution for both climate change mitigation and the production of high-value chemicals from  $\text{CO}_2$ . The growing number of publications and citations reflects the increasing recognition of this technology's significance and its promise for both scientific and practical applications (Fig. 2). A key challenge remains optimizing selectivity and efficiency in  $\text{C}_{2+}$  hydrocarbon production, which is essential for scaling these systems. Ultimately, this research not only enhances our understanding of solar-driven catalysis but also contributes to the development of carbon-neutral technologies, with substantial implications for sustainable chemical manufacturing and global sustainability goals.

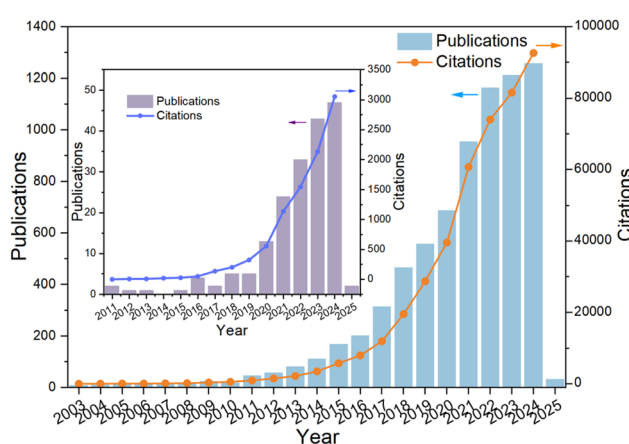
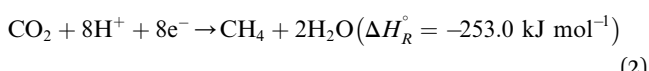


Fig. 2 The number of publications and citations from Web of Science on photo-driven catalytic  $\text{CO}_2$  reduction, encompassing all product types, has surged in recent years; the illustration focuses specifically on  $\text{CO}_2$  conversion into  $\text{C}_{2+}$  products.

## 1.2 Mechanism of photothermal conversion of $\text{CO}_2$ into $\text{C}_{2+}$ products

Photo-driven direct conversion of  $\text{CO}_2$  to  $\text{C}_{2+}$  as major products, either saturated or unsaturated hydrocarbons or oxygenated products, such as light olefins ( $\text{C}_{2-4}=\text{}$ ), paraffins ( $\text{C}_{2-4}^0$ ),  $\text{C}_{2+}$  alcohol, carboxylic acid, and dimethyl carbonate, would be much more attractive, considering the higher market price per ton of these  $\text{C}_{2+}$  compounds, compared to the  $\text{C}_1$  products.<sup>57</sup>

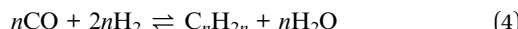
Hydrogenation of  $\text{CO}_2$  to form various products is an exothermic process, where the exact is dependent on the product. Eqn (1) and (2) summarize the redox reactions of commonly reported  $\text{C}_1$  products of the photocatalytic  $\text{CO}_2$  reduction.



The high added  $\text{C}_{2+}$  chemicals with multiple carbon atoms are more attractive than  $\text{C}_1$  products because they have a higher energy density. Hydrogenation of  $\text{CO}_2$  to  $\text{C}_{2+}$  products can be achieved through two different paths.<sup>58</sup> The first is the direct  $\text{CO}_2$  Fischer-Tropsch synthesis pathway; the second is the indirect methanol-mediated pathway, where  $\text{CO}_2$  is first converted to  $\text{CH}_3\text{OH}$ , which is subsequently transformed into  $\text{C}_{2+}$  products through reactions such as dehydration, oligomerization, and hydrogenation. The direct pathway is the  $\text{CO}_2$ -Fischer-Tropsch ( $\text{CO}_2$ -FT) path:  $\text{CO}_2$  and  $\text{H}_2$  undergo reverse water gas conversion (RWGS) reaction to form the intermediate  $\text{CO}$ , followed by Fischer-Tropsch synthesis reaction (FTS). In the following  $\text{CO}_2$ -FT reaction,  $\text{C}_1$  intermediates undergo C–C coupling and hydrogenation to form  $\text{C}_{2+}$  products. C–C coupling intermediates play a crucial role in the synthesis of  $\text{C}_{2+}$  hydrocarbons. Due to the complexity of intermediates and diverse reaction pathways, uncovering the reaction mechanisms of  $\text{C}_{2+}$  hydrocarbons remains a significant challenge.<sup>59–61</sup> However, the chain growth pathway in FTS remains controversial. Two proposed mechanisms are  $\text{CH}_x$  insertion (carbide type)<sup>62</sup> and “CO” insertion.<sup>63</sup> The  $\text{CH}_x$  insertion assumes  $\text{CO}$  activation either by direct reaction with chemisorbed hydrogen or *via* an H-assisted pathway, possibly through formyl ( $\text{HCO}^*$ ), formaldehyde ( $\text{H}_2\text{CO}^*$ ), or hydroxymethylene ( $\text{HCOH}^*$ ) species, to form surface  $\text{CH}_x^*$ .

Direct  $\text{CO}$  activation removes  $\text{O}^*$  from  $\text{CO}_2$ , while H-assisted  $\text{CO}$  dissociation forms  $\text{H}_2\text{O}$  exclusively. In the CO insertion mechanism,  $-\text{CH}_x^*$  species are believed to couple with  $\text{CO}^*$  to form  $-\text{CH}_2\text{CO}^*$ , facilitated by surface OH groups, followed by deoxyhydrogenation of the oxygen intermediate.<sup>63</sup> The main reaction is as follows eqn (3)–(5). Considering the optimal catalyst strategy, the different electron distribution and valence state of two different metal active sites at the interface may cause the charge distribution of the  $\text{C}_1$  intermediate to be significantly different, thus reducing the  $\text{C}_1$  electrostatic repulsion, promoting the C–C coupling reaction. Ning *et al.* have successfully developed a  $\text{Co}^0\text{--Co}^{\delta+}$  double active centre catalyst

supported on  $\text{MgAl}_2\text{O}_4$  (Co-CoO<sub>x</sub>/MAO) for the efficient conversion of CO<sub>2</sub> into C<sub>2-4</sub> olefins by photothermocatalysis.<sup>9</sup>



The indirect pathway is methanol-mediated, where CO<sub>2</sub> and hydrogen are first converted to CH<sub>3</sub>OH, followed by methanol-to-olefin reaction (MTO). The stoichiometric reaction of CO<sub>2</sub> hydrogenation to CH<sub>3</sub>OH is shown in eqn (6) and (7). This reaction pathway has been recognized over bifunctional systems comprising a CH<sub>3</sub>OH synthesis catalyst and a methanol-to-hydrocarbon (MTH) catalyst. Li *et al.*<sup>64</sup> proposed the use of a ZnZrO/SAPO tandem catalyst for the direct hydrogenation of CO<sub>2</sub> to produce light olefins. In mechanistic studies, *in situ* diffuse reflectance infrared Fourier-transform spectroscopy (DRIFTS) was used to detect surface species formed on ZnZrO and the tandem catalyst. Quantitative analysis using chemical trapping-mass spectrometry revealed that the intensity of CH<sub>3</sub>O\* on the tandem catalyst was lower than on ZnZrO, but chemical trapping produced strong mass signals for CD<sub>3</sub>CHO and CH<sub>3</sub>OCD<sub>3</sub>, indicating that CHO\* and CH<sub>3</sub>O\* species were more actively involved in the reaction (Fig. 3a and b). These results suggest that these derived CH<sub>x</sub>O species migrate into the zinc-modified SAPO-34 zeolite, where they are converted into lower olefins (Fig. 3c).



Ethanol is arguably available CO<sub>2</sub> hydrogenation C<sub>2</sub> product due to its safe transport and higher calorific value.<sup>68</sup> The process of CO<sub>2</sub> hydrogenation to ethanol includes CO<sub>2</sub> to produce CO by reverse water-gas conversion reaction, partial CO dissociation to produce  $-\text{CH}_3^*$  group, CO embedding into  $-\text{CH}_3^*$  to complete carbon chain growth, and further hydrogenation to produce ethanol.<sup>69,70</sup> Therefore, the ethanol synthesis catalyst requires the following functional sites, H<sub>2</sub> dissociation, CO dissociation adsorption site, CO non-dissociation adsorption site, and C–C coupling site. The reaction formula of CO<sub>2</sub> catalytic hydrogenation to ethanol is shown in eqn (8).



In a continuous reactor, Yang *et al.* explored the key role of hydroxyl in Rh-based catalysts supported on TiO<sub>2</sub> nanorods (Fig. 3b). The results show that the ethanol selectivity of RhFeLi/TiO<sub>2</sub> nanorods is 32% in the catalytic CO<sub>2</sub> hydrogenation reaction. The promotion effect can be attributed to the highly dispersed Rh and high density  $^*\text{CH}_x$  on the TiO<sub>2</sub> nanorods, and then CO (generated by RWGS reaction) is inserted into  $^*\text{CH}_x$  to form  $^*\text{CH}_3\text{CO}$ , and  $^*\text{CH}_3\text{CO}$  is hydrogenated to produce ethanol.<sup>65</sup>

Acetic acid is an important commodity chemical, mainly used as a raw material for the production of vinyl acetate

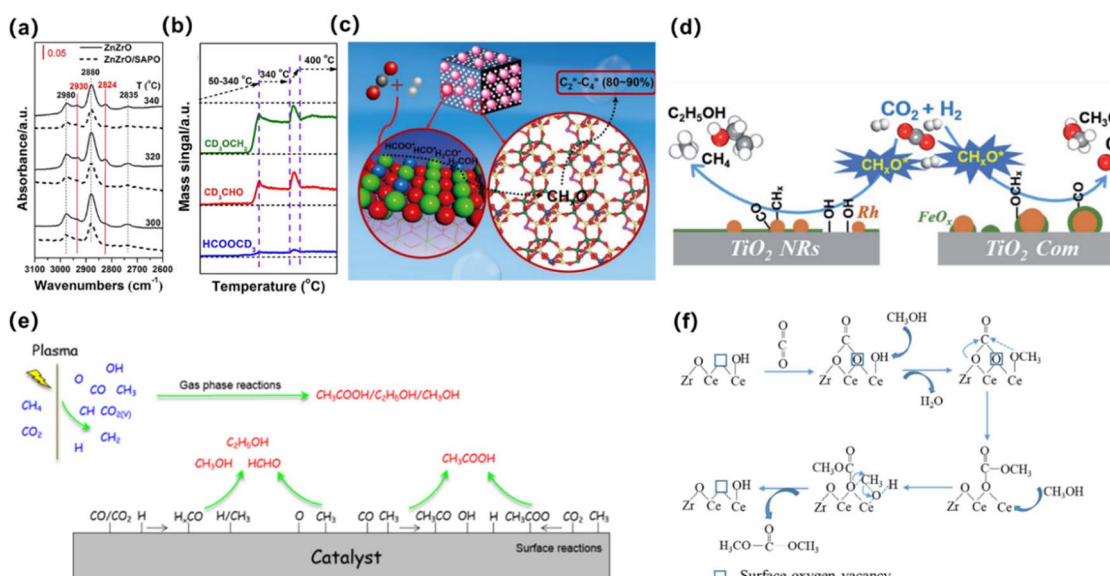


Fig. 3 (a) *In situ* DRIFT spectra from CO<sub>2</sub> hydrogenation over ZnZrO and ZnZrO/SAPO at different temperatures. (b) Chemical trapping-mass spectrometry results with a trapping reagent CD<sub>3</sub>OD during the CO<sub>2</sub> hydrogenation over ZnZrO at reaction temperatures of 50–400 °C. (c) Schematic for the proposed reaction mechanism of CO<sub>2</sub> hydrogenation on the tandem catalyst, ZnZrO/SAPO.<sup>64</sup> Copyright 2017, American Chemical Society. (d) Schematic of CO<sub>2</sub> hydrogenation over the Rh-based catalyst with or without hydroxyl groups on TiO<sub>2</sub>. The hydroxyls play an important role in accelerating the scission of CH<sub>x</sub>O\* and promote the formation of ethanol.<sup>65</sup> Copyright 2019, Royal Society of Chemistry. (e) Possible reaction mechanisms for the formation of CH<sub>3</sub>COOH, CH<sub>3</sub>OH, C<sub>2</sub>H<sub>5</sub>OH and HCHO using the plasma-catalysis approach.<sup>66</sup> Copyright 2017, Royal Society of Chemistry. (f) Oxygen vacancy promoting dimethyl carbonate synthesis from CO<sub>2</sub> and CH<sub>3</sub>OH over Zr-doped CeO<sub>2</sub> nanorods.<sup>67</sup> Copyright 2018, Royal Society of Chemistry.



monomer, ethyl acetate, propyl acetate, *n*-butyl acetate, isobutyl acetate and acetic anhydride, or as a solvent in the synthesis of terephthalic acid.<sup>71</sup>

It is generally believed that the catalytic mechanism of direct synthesis of acetic acid by coupling  $\text{CH}_4$  and  $\text{CO}_2$  consists of 5 steps (eqn (9)–(13)): (1)  $\text{CH}_4$  dissociates on the catalyst surface to form methylated species ( $\text{M}-\text{CH}_3$ ) and a Brønsted proton; (2)  $\text{CO}_2$  is adsorbed on the surface of the catalyst to produce surface adsorbed species  $\text{CO}_2^*$  (on some catalysts, the gas phase  $\text{CO}_2$  can be directly inserted into the  $\text{M}-\text{CH}_3$  bond, without this step); (3)  $\text{CO}_2^*$  is inserted into  $\text{M}-\text{CH}_3$  bond (C–C coupling) to generate surface acetate species; (4) Brønsted protons on the surface acetate species extraction carrier form acetic acid adsorption species; (5) acetic acid adsorbed species desorption to produce acetic acid.<sup>72–76</sup>



Tu *et al.* adopted a new atmospheric pressure reactor to achieve the one-step synthesis of liquid fuels and chemicals at room temperature by direct reforming of  $\text{CO}_2$  and  $\text{CH}_4$  (Fig. 3c). The overall selectivity for liquid chemicals is about 50–60%, and the main product is acetic acid. The molar ratio of  $\text{CH}_4/\text{CO}_2$  and the type of catalyst can control the formation of different oxygenates.<sup>66</sup>

Dimethyl carbonate (DMC) is known as the “new base block” of organic synthesis in the 21st century, which can replace toxic phosgene, dimethyl sulfate, chloromethane and other reagents for methylation, carbonylation, methoxylation and other reactions, and is used to synthesize a variety of important fine chemicals.<sup>77</sup> From a green chemistry point of view, direct synthesis of DMC from  $\text{CO}_2$  and  $\text{MeOH}$  is a better route because the raw material ( $\text{MeOH}$ ) is relatively cheap and the main by-product is water ( $\text{H}_2\text{O}$ ).<sup>78</sup> The reaction formula is as follows:



At present, although there are many studies on the catalytic mechanism of  $\text{CH}_3\text{OH}$  and  $\text{CO}_2$  synthesis of DMC, it can be basically summarized into two types: the reaction mechanism of direct activation of  $\text{CO}_2$  and the reaction mechanism of first activation of  $\text{CH}_3\text{OH}$  and then activation of  $\text{CO}_2$ .

Catalytic mechanism of direct activation of  $\text{CO}_2$ : the catalyst provides electrons to the  $\pi$  orbital of  $\text{CO}_2$  molecules, resulting in the bending of its molecular structure, and with the extension of C–O bonds, the formation of  $[\text{CO}_2^-]$ , thus realizing the activation of  $\text{CO}_2$ , and further coupling with  $\text{CH}_3\text{OH}$  to produce DMC under the synergistic action of the catalyst. The catalytic

mechanism of the first activation of  $\text{CH}_3\text{OH}$  and then activation of  $\text{CO}_2$  is that the catalyst causes  $\text{CH}_3\text{OH}$  to lose protons to form  $[\text{MeO}]^-$ , and then combines with  $\text{CO}_2$  to form  $[\text{MeOCOO}]^-$ , and then the methyl group is transferred to form DMC. Li *et al.* synthesized a series of ZR-doped  $\text{CeO}_2$  nanorods by hydrothermal method (Fig. 3d), and studied in detail the effect of the doping content of Zr on the lattice structure, microstructure, especially the amount of oxygen vacancy as well as the catalytic activity of DMC synthesis from  $\text{CO}_2$  and  $\text{CH}_3\text{OH}$  were studied in detail.<sup>67</sup>

## 2. Catalyst design for solar-driven catalytic $\text{C}_2+$ product synthesis

### 2.1 Surface defect engineering

The generation of surface defects such as oxygen vacancies (OVs), interstitial defects, or cation states has been widely reported to enhance photo-driven catalytic activity.<sup>79–82</sup> Oxygen vacancy engineering significantly enhances  $\text{CO}_2$  reduction performance by optimizing electronic structures and charge separation. Ye and co-workers achieved self-doped  $\text{SrTiO}_{3-\delta}$  photocatalysts exhibit improved visible light absorption and charge mobility due to oxygen vacancies.<sup>79</sup> Similarly, ultrathin  $\text{W}_{18}\text{O}_{49}$  nanowires with abundant vacancies enhance  $\text{CO}_2$  activation and photochemical reduction efficiency.<sup>80</sup> Furthermore, cation vacancies in  $\text{ZnS}$  enhance  $\text{CO}_2$  reduction by providing stable active sites that facilitate charge separation and  $\text{CO}_2$  adsorption. Unlike anion vacancies, they resist oxygen refilling, maintaining activity and promoting intermediates formation for improved  $\text{CO}_2$  photoreduction efficiency.<sup>81,82</sup>

High temperature treatment in hydrogen atmosphere has been regarded as a powerful method for surface defect preparation, especially for oxygen vacancies. After the pioneering method was developed. Mao's team, it has been successfully used for oxygen vacancy introduction in a variety of metal oxide systems.<sup>83</sup> As shown in the (Fig. 4a), during the high-temperature treatment process, hydrogen reduces  $\text{TiO}_2$  to other chemical substances, and a partially disordered structure can be found on the surface, and  $\text{Ti}^{4+}$  will become  $\text{Ti}^{3+}$  and form oxygen vacancy. This hydrogenation process will make the color of  $\text{TiO}_2$  change from white to black (Fig. 4b), greatly improving the light absorption range and enhancing the catalytic activity.

According to this method, Durrant *et al.* reported  $\text{CH}_4$  and ethane production using Pt-sensitized graphene-wrapped defect-induced  $\text{TiO}_2$  photocatalysts under sun-simulated light irradiation (Fig. 4c). In this example,  $\text{TiO}_2$  NPs were reduced with sodium borohydride at 350 °C in an argon atmosphere, creating defect-induced  $\text{TiO}_2$  with midgap states ( $\text{Ti}^{3+}$ ). The defect-induced  $\text{TiO}_2$  was then mixed with GO and annealed at 230 °C in a vacuum oven. Finally, Pt NPs were photo-deposited from  $\text{H}_2\text{PtCl}_6$  aqueous solution with  $\text{MeOH}$  as a sacrificial agent. The authors proposed that the synergy between surface- $\text{Ti}^{3+}$  sites and wrapped graphene enhanced ethane formation.<sup>82</sup>

Tatsumi Ishihara *et al.* reported the first synthesis of ultrathin  $\text{WO}_3$  0.33 $\text{H}_2\text{O}$  nanotubes with a large amount of exposed surface  $\text{Vo}$  sites, achieving excellent and stable  $\text{CO}_2$



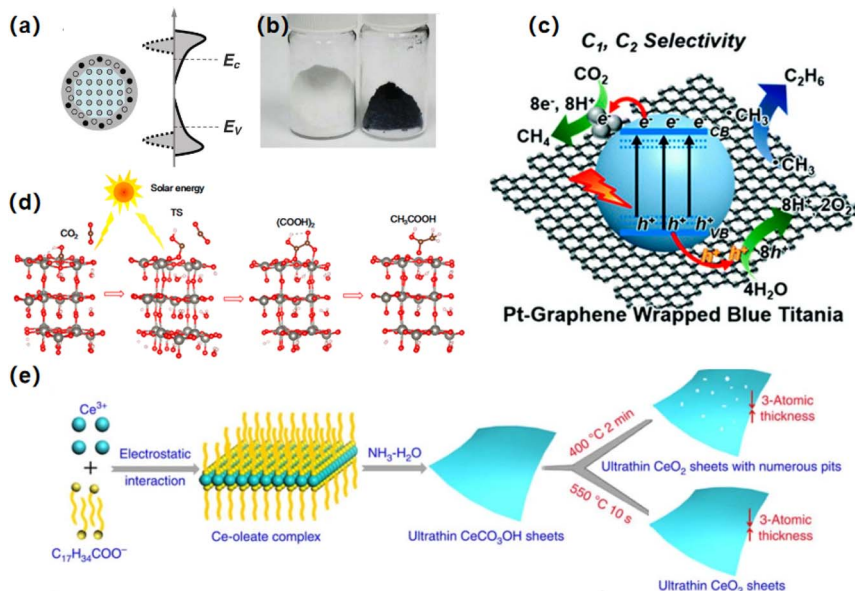


Fig. 4 (a) Schematic illustration of the concept to make black  $\text{TiO}_2$ . (b) Pictures of white and black  $\text{TiO}_2$  nanomaterials.<sup>83</sup> Copyright 2011, American Association for the Advancement of Science. (c) Pt-sensitized graphene-wrapped RBT.<sup>82</sup> Copyright 2018, Royal Society of Chemistry. (d) Possible main reaction paths for acetic acid generation on ultrathin  $\text{WO}_3 \cdot 0.33\text{H}_2\text{O}$  nanotubes.<sup>84</sup> Copyright 2018, American Chemical Society. (e) Schematic illustration for the formation of  $\text{V}_\text{O}$ -rich/poor atomically thin  $\text{In}_2\text{O}_3$  porous sheets at different atmosphere.<sup>85</sup> Copyright 2014, American Chemical Society.

photoreduction to  $\text{CH}_3\text{COOH}$  in pure water under solar light (Fig. 4d). The selectivity for acetic acid is up to 85%, with an average productivity of about  $9.4 \mu\text{mol g}^{-1} \text{h}^{-1}$ . Importantly,  $\text{V}_\text{O}$  sites in the catalyst remained stable, with their concentration unchanged even after 60 hours of reaction. Quantum chemical calculations and *in situ* DRIFT studies revealed the main reaction pathway:  $\text{CO}_2 \rightarrow \cdot\text{COOH} \rightarrow (\text{COOH})_2 \rightarrow \text{CH}_3\text{COOH}$ .<sup>84</sup>

Xie *et al.*<sup>85</sup> have developed a rapid heating phase transition method to create defects, or oxygen vacancies, on the surface of two-dimensional materials. Using  $\text{CeCO}_3\text{OH}$ ,  $\text{In}(\text{OH})_3$ ,  $\text{WO}_3 \cdot x\text{H}_2\text{O}$ , and cobaltous oxide ultra-thin nanosheets as precursors, the researchers prepared cerium oxide,  $\text{In}_2\text{O}_3$ , tungsten trioxide, and  $\text{Co}_3\text{O}_4$  ultra-thin nanosheets through the phase transformation process (Fig. 4e). This method endows these materials with a narrowed band gap and higher carrier concentration, thereby enhancing visible light harvesting and improving carrier separation efficiency.<sup>85-88</sup>

Chemical reduction is an effective method for introducing surface defects into semiconductor materials. This can be achieved using reducing agents such as  $\text{NaBH}_4$ , calcium hydride, and hydrazine, or reducing solvents like glycol and glycerol.<sup>89-91</sup> When metal oxides are prepared using reducing solvents, the material typically loses oxygen atoms, creating oxygen vacancies. For example, in  $\text{BiOCl}$ , ethylene glycol reacts with oxygen atoms on the  $\text{BiOCl}$  (001) surface at  $160^\circ\text{C}$ , forming oxygen vacancies. These vacancies extend the photo-absorption edge of the catalyst to visible light, enhance its ability to trap photogenerated electrons, and enable it to activate oxygen molecules to produce free radicals.<sup>92</sup>

Surface defect engineering provides a flexible and effective method to improve catalytic performance by selectively

introducing or optimizing defect structures on the catalyst surface. This provides a new way to design more efficient and selective catalysts, and plays an important role in the research and application of catalytic  $\text{CO}_2$ .

## 2.2 Bifunctional active sites design

The photo-driven hydrogenation of  $\text{CO}_2$  to produce  $\text{C}_1$  products like  $\text{CO}$  and  $\text{CH}_4$  has been extensively studied. However, methods for  $\text{CO}_2$  reduction to  $\text{C}_{2+}$  products show low activity and selectivity. In photothermal-catalytic systems, enhancing  $\text{C}_{2+}$  product generation while suppressing  $\text{C}_1$  formation remains challenging. This is because forming  $\text{C}_{2+}$  products requires C–C coupling reactions between intermediates, which face higher reaction barriers than C–H bond formation. Typically, the selectivity for  $\text{C}_2\text{–C}_4$  hydrocarbons and  $\text{C}_{5+}$  hydrocarbons is limited to 58% and 48%,<sup>93</sup> respectively, due to the Anderson–Schulz–Flory (ASF) distribution, significantly limiting  $\text{C}_{2+}$  production.

Efficiently producing  $\text{C}_{2+}$  products requires high-selectivity C–C coupling in the  $\text{CO}_2$  reduction reaction. Catalysts with bifunctional active sites can overcome this limitation. Depending on the reaction pathway, such as the modified FTS pathway or the  $\text{CH}_3\text{OH}$  pathway, the bifunctional catalyst components play different roles in producing value-added products, thus breaking the ASF distribution.<sup>94</sup> Therefore, designing and regulating catalytic active sites for C–C coupling provides insights into creating catalysts that produce  $\text{C}_{2+}$  products other than  $\text{CO}$ . Bifunctional catalysts are classified based on the source and configuration of their active sites: heteronuclear multi-active sites, homonuclear multi-active



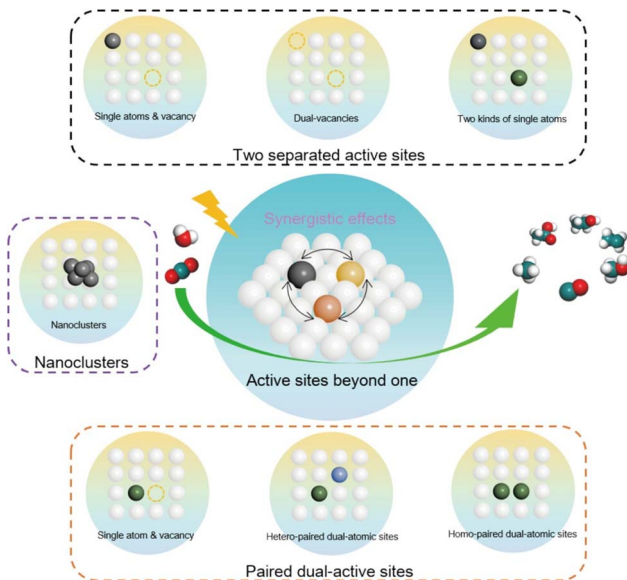


Fig. 5 Representative categories of photo-driven  $\text{CO}_2$  reduction multi-active sites.<sup>95</sup> Copyright 2014, Springer.

sites, and combined integration of two kinds of active sites (Fig. 5).<sup>95</sup> The first two types refer to catalysts composed of two adjacent active sites, differing in whether the active sites are the same. The third type involves randomly distributed homonuclear dual active sites.

Homonuclear multi-active site catalysts refer to identical and adjacent active sites embedded in a support structure, where

the two active sites can interact by modulating the local electronic structure. This interaction results in different or similar structural behaviors. Ye *et al.* utilized a  $\text{Co}^0$  and  $\text{Co}^{\delta+}$  dual active center catalyst supported on  $\text{MgAl}_2\text{O}_4$  ( $\text{Co}-\text{CoO}_x/\text{MAO}$ ) for the efficient photothermal catalytic conversion of  $\text{CO}_2$  to  $\text{C}_{2-4}$  olefins.<sup>9</sup> In this system,  $\text{Co}^0$  sites effectively adsorb and activate  $\text{CO}_2$  to produce  $\text{C}_1$  intermediates, while the electron-deficient  $\text{Co}^{\delta+}$  sites reduce the energy barrier for the critical  $\text{CHCH}^*$  intermediate, promoting the formation of  $\text{C}_{2-4}$  olefins. Compared to the  $\text{Co}/\text{MAO}$  catalyst, the  $\text{Co}-\text{CoO}_x/\text{MAO}$  catalyst with dual active sites produces a substantial amount of multi-carbon products in the  $\text{CO}_2$  hydrogenation products (Fig. 6a). The activity for  $\text{C}_{2-4}$  hydrocarbons reached as high as  $1303 \mu\text{mol g}^{-1} \text{h}^{-1}$ . Additionally, using the same synthesis procedure, Co species were loaded onto  $\text{TiO}_2$  and  $\text{Al}_2\text{O}_3$ . The cobalt species on different supports exhibited similar product distributions in  $\text{CO}_2$  hydrogenation under identical reaction conditions (Fig. 6b), indicating the general applicability of the  $\text{Co}^0-\text{Co}^{\delta+}$  site design concept.

In contrast to homonuclear multi-active sites, heteronuclear multi-active sites have distinct active sites with varying electronic structures, making them potentially effective photocatalysts for  $\text{CO}_2$  reduction reaction ( $\text{CO}_2\text{RR}$ ). The electronic structure of such catalysts can be suitably tuned through synergistic effects, resulting in enhanced performance. Jia *et al.*<sup>96</sup> synthesized a Ni and Co co-loaded  $\text{TiO}_2$  photocatalyst ( $\text{NiCo}-\text{TiO}_2$ ). The dual Ni and Co sites replace adjacent Ti atoms in the  $\text{TiO}_2$  lattice, forming an asymmetric dual-atom site photocatalyst. The asymmetric local electric field generated by the dual-atom sites creates asymmetric charge centers,

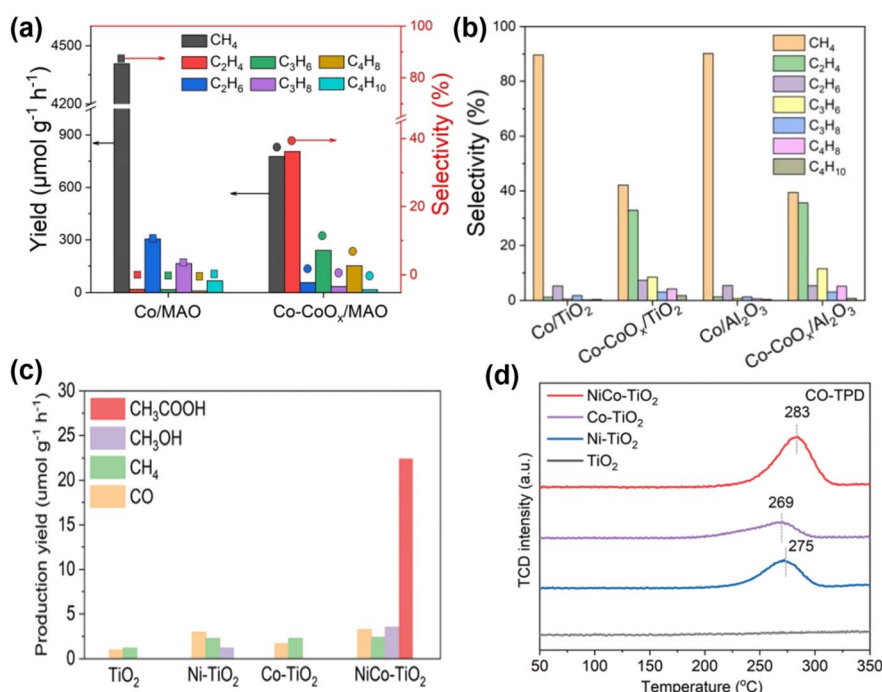


Fig. 6 (a) Product yield and selectivity of  $\text{CO}_2$  hydrogenation in a closed gas circulation system. (b) Product selectivity relative to other catalysts.<sup>9</sup> Copyright 2023, Wiley. (c) Yield of  $\text{CH}_3\text{COOH}$  and other products under UV-visible light irradiation. (d) CO-TPD spectra of  $\text{NiCo-TiO}_2$ ,  $\text{Ni-TiO}_2$ ,  $\text{Co-TiO}_2$  and  $\text{TiO}_2$ .<sup>96</sup> Copyright 2022, Wiley-VCH Verlag.



promoting the separation of photogenerated carriers and facilitating multi-electron processes. This accelerates the CO<sub>2</sub>RR reaction, leading to high selectivity and activity for CH<sub>3</sub>COOH production. Photocatalytic CO<sub>2</sub> reduction results show that CH<sub>3</sub>COOH is a major product for NiCo-TiO<sub>2</sub>, while the original TiO<sub>2</sub>, Ni-TiO<sub>2</sub>, and Co-TiO<sub>2</sub> predominantly produce C1 species (Fig. 6c). Compared with Ni-TiO<sub>2</sub> and Co-TiO<sub>2</sub>, the CO-TPD signal of NiCo-TiO<sub>2</sub> shifts to higher temperatures, indicating superior chemisorption capacity in the dual-site state, mainly due to the electronic interaction of the bimetal, which promotes the formation of C<sub>2+</sub> products post-coupling (Fig. 6d).

Two separate active sites are randomly distributed on the support, with some interconnected, offering unique advantages in CO<sub>2</sub>RR due to synergistic effects. Integrating different single atoms into the support enables synergistic catalysis in CO<sub>2</sub> activation. For example, Wang *et al.*<sup>97</sup> introduced P and Cu onto carbon nitride nanosheets, forming P-N and Cu-N<sub>4</sub> dual active sites (P/Cu SAs@CN), achieving efficient carrier separation for photocatalytic CO<sub>2</sub>RR to produce C<sub>2</sub>H<sub>6</sub>. The dual active sites significantly enhanced CO<sub>2</sub> reduction performance, with a C<sub>2</sub>H<sub>6</sub> yield of 616.6  $\mu\text{mol g}^{-1} \text{h}^{-1}$ , 26 times higher than Cu SAs@CN, highlighting the crucial role of P in C<sub>2</sub>H<sub>6</sub> production (Fig. 7a and b). Quasi-*in situ* XPS showed a positive shift of P<sub>2p</sub> after light irradiation on P/Cu SAs@CN, indicating P atoms' role in hole capture. P atoms capture photo-generated holes, aiding electron accumulation at Cu sites and enabling multi-electron transfer in CO<sub>2</sub>RR (Fig. 7c). Theoretical analysis shows electron-enriched Cu sites have a lower energy barrier for C-C coupling under light, favoring CO<sub>2</sub>RR and C<sub>2</sub>H<sub>6</sub> formation. CO<sub>2</sub> adsorbed onto

Cu sites reduces to CO\*, and then desorbed, while the rest forms CH<sub>4</sub> and C<sub>2</sub>H<sub>6</sub> through electron transfer and hydrogenation steps, with \*OCCO to \*OC-COH as key steps (Fig. 7d).

### 2.3 Coupling catalytic effect of co-catalyst

Compared to typical surface catalytic reactions, the transfer of photogenerated carriers to the surface occurs much more rapidly, leading to the accumulation of interfacial charges.<sup>98</sup> Reduced charge separation rates and increased reaction overpotentials result in poorer overall photocatalytic performance. Loading suitable co-catalysts can lower the overpotential of redox reactions, enhance electron–hole pair (EHP) separation at the interface, inhibit photodegradation, and ultimately improve photostability.<sup>99,100</sup>

In semiconductor-cocatalyst composite systems, the electron dynamics during CO<sub>2</sub> photoreduction can be divided into four processes (Fig. 8): (1) excitation of the semiconductor. (2) Transfer of photogenerated electrons from the semiconductor through the junction to the co-catalyst and coupling its hot electrons. (3) Transfer of photogenerated/hot electrons to the active sites of the co-catalyst. (4) Surface redox reactions at the active sites.<sup>101</sup> Efficient electrons migration from the catalyst surface to the co-catalyst addresses issues such as significant carrier recombination, low solar energy utilization, and photocatalyst photodegradation.

Co-catalysts enhance charge separation in photo-driven catalytic reactions by acting as sinks for photogenerated electrons (e<sup>-</sup>) or holes (h<sup>+</sup>), and coupling photothermal conversion at the composite sites. Li *et al.* modified ultrathin porous g-C<sub>3</sub>N<sub>4</sub> nanosheets with AuCu alloy nanoparticles.<sup>102</sup> These AuCu NPs

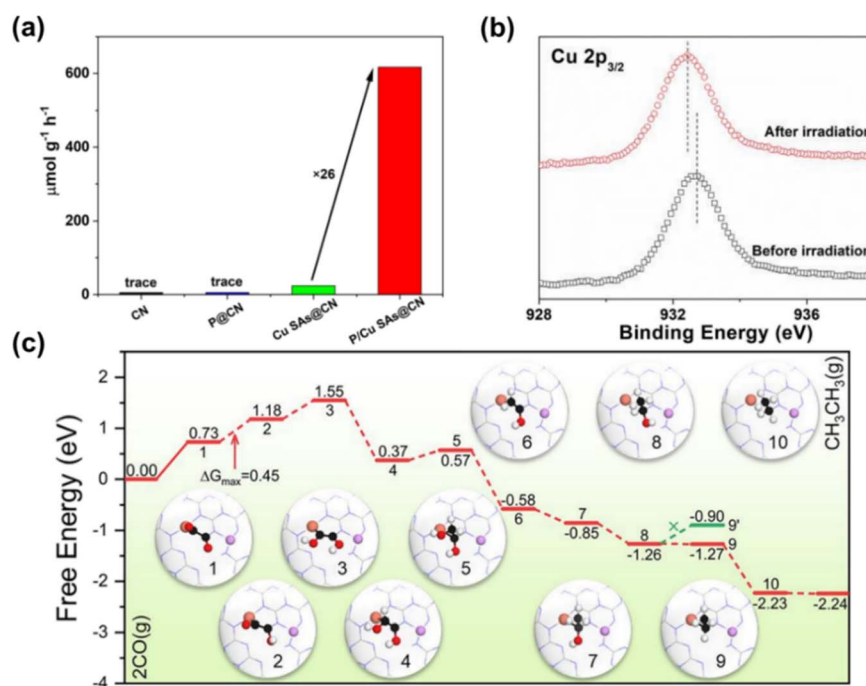


Fig. 7 (a) Photo-driven CO<sub>2</sub>RR generates C<sub>2</sub>H<sub>6</sub> on CN, P@CN, CuSAs@CN and P/Cu SAs@CN. (b) Cu 2p<sub>3/2</sub> over P/Cu SAs@CN before and after light irradiation. (c) Free energy diagram of CO coupling reduction to C<sub>2</sub> products on P/Cu SAs@CN photocatalyst and atomic structure of reaction intermediates.<sup>97</sup> Copyright 2022, Wiley.

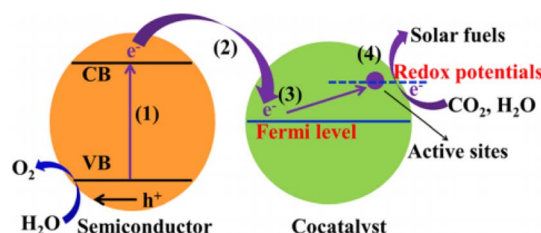


Fig. 8 Typical process of semiconductor-cocatalyst composite system in  $\text{CO}_2$  photoreduction process.<sup>101</sup> Copyright 2019, American Chemical Society.

facilitate rapid charge separation and partially activate  $\text{CO}_2$  molecules, aiding  $\text{CO}_2$  reduction. The local surface plasmon resonance (LSPR) of Au enhances light absorption and light-to-heat conversion, and promotes C-C coupling during ethanol formation. Transient photocurrent responses show that  $\text{Cu/g-C}_3\text{N}_4$ ,  $\text{Au/g-C}_3\text{N}_4$ , and  $\text{AuCu/g-C}_3\text{N}_4$  electrodes produce higher photocurrents than  $\text{g-C}_3\text{N}_4$  alone, with  $\text{AuCu/g-C}_3\text{N}_4$  showing the highest, six times greater than  $\text{g-C}_3\text{N}_4$  (Fig. 9a), suggesting that AuCu nanoparticles significantly improve charge separation efficiency. Photothermal catalytic tests show increased activity of metal-loaded catalysts at 120 °C, particularly boosting ethanol yield on  $\text{AuCu/g-C}_3\text{N}_4$  (Fig. 9b). The proposed mechanism for ethanol production involves photogenerated electrons and holes in  $\text{g-C}_3\text{N}_4$  transferring to AuCu NPs under light. Positive charges on Au enhance  $\text{CO}_2$  adsorption, while charge transfer from Au to Cu enriches Cu with negative charges, promoting  $\text{CO}_2^-$  and  ${}^*\text{CO}$  formation on Cu. Elevated temperatures enhance molecular motion, creating a synergistic effect between photocatalysis and thermocatalysis, promoting  ${}^*\text{CO}$  dimerization and increasing  $\text{CH}_3\text{CH}_2\text{OH}$  yield (Fig. 9c).

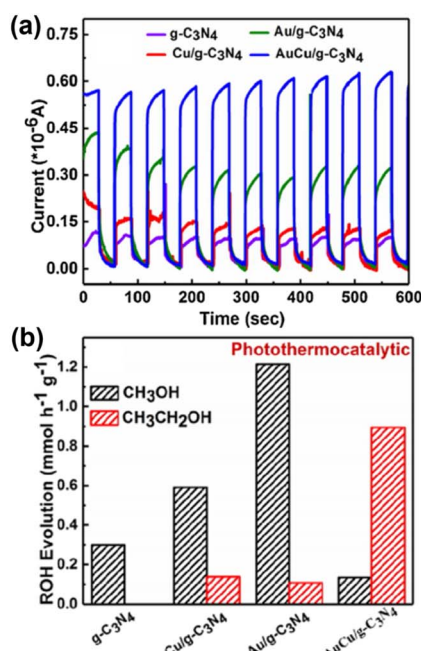


Fig. 9 (a) Photocurrent response of  $\text{g-C}_3\text{N}_4$  nanosheets,  $\text{Cu/g-C}_3\text{N}_4$ ,  $\text{Au/g-C}_3\text{N}_4$  and  $\text{AuCu/g-C}_3\text{N}_4$  nanocomposites. (b) Photothermal catalytic reduction of  $\text{CO}_2$  performance (PTCR: 120 °C). (c) Schematic diagram of PTCR conversion of  $\text{CO}_2$  into ethanol via  $\text{AuCu/g-C}_3\text{N}_4$  nanocomposite catalyst.<sup>102</sup> Copyright 2020, Elsevier.

The accumulation of photogenerated/hot electrons and holes on co-catalyst nanoparticles (NPs) leads to  $\text{C}_{2+}$  products formation through semiconductor interactions. Ji *et al.* developed  $\text{Au-CeO}_2$  nanocomposites with  $\text{Au-O-Ce}$  sites, enabling selective photocatalytic  $\text{CO}_2$  conversion to ethane.<sup>103</sup> The  $\text{Au-CeO}_2$  interface ensures multi-electron reduction of  $\text{CO}^*$ , enhancing  $\text{CO}_2$  conversion. Pristine  $\text{CeO}_2$  shows a CO yield of  $2.02 \mu\text{mol g}^{-1} \text{h}^{-1}$  with no  $\text{C}_2\text{H}_6$  over 4 hours. Increasing Au component shifts the primary product from CO to  $\text{C}_2\text{H}_6$ , peaking at 3 wt% Au with yields of  $5.88$  and  $11.07 \mu\text{mol g}^{-1} \text{h}^{-1}$  for CO and  $\text{C}_2\text{H}_6$ , respectively (Fig. 10a). *In situ* FTIR reveals crucial  $\text{C}_{2+}$  intermediates like  $\text{COCO}^*$  and  $\text{COCOH}^*$  (Fig. 10b), absent in pristine  $\text{CeO}_2$ , indicating the importance of the  $\text{Au-CeO}_2$  interface. Gibbs free energy (Fig. 10c) calculations show that the  $\text{Au-CeO}_2$  interface lowers the  $\text{COOH}^*$  formation barrier from 1.09 eV to 0.50 eV, favoring  $\text{COCO}^*$  formation over CO desorption. This reduction in energy barriers is key to producing  $\text{C}_2\text{H}_6$ , confirming the critical role of the  $\text{Au-O-Ce}$  interface in  $\text{CO}_2$  reduction to  $\text{C}_{2+}$  products.

### 3. Solar-energy mediated $\text{CO}_2$ reduction reactions

The catalytic conversion of  $\text{CO}_2$  into value-added  $\text{C}_1$  products such as CO,  $\text{CH}_4$ , and  $\text{CH}_3\text{OH}$  has emerged as a promising approach for mitigating carbon emissions.<sup>104–106</sup> This strategy is closely aligned with the principles of green circular economy and environmental sustainability. Despite its potential, the primary challenge remains in enhancing the efficiency and selectivity of  $\text{CO}_2$  conversion processes to produce high-value products on an industrial scale. This review highlights recent

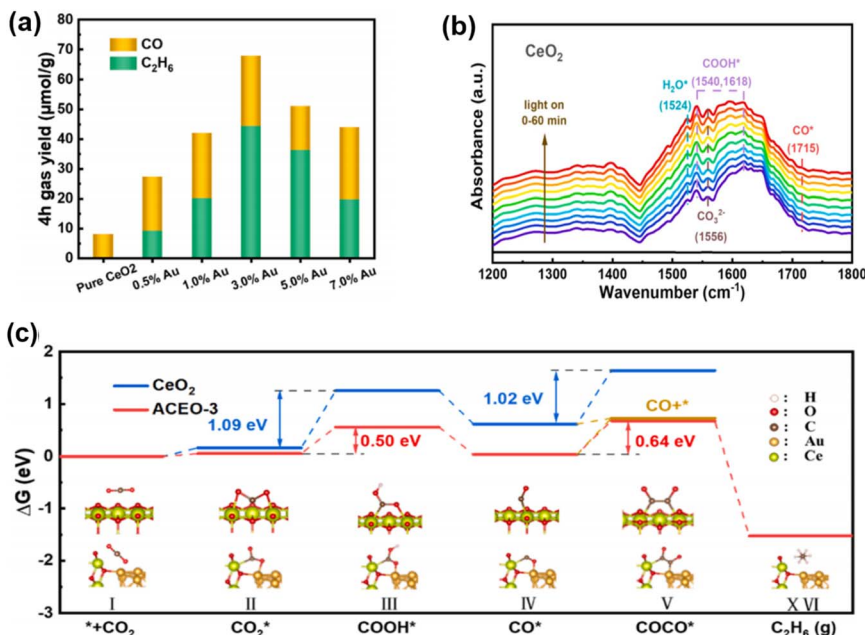


Fig. 10 (a) CO and C<sub>2</sub>H<sub>6</sub> generation rates as a function of Au content; *in situ* FTIR spectra of CO<sub>2</sub> and H<sub>2</sub>O vapor mixtures co-adsorbed on (b) CeO<sub>2</sub>. (c) Reaction pathway for Gibbs free energy calculation of photocatalytic CO<sub>2</sub> reduction.<sup>103</sup> Copyright 2023, Elsevier.

advancements in photothermal catalytic systems for CO<sub>2</sub> conversion, with a focus on not only the production of C<sub>1</sub> compounds but also the synthesis of more complex and economically significant C<sub>2+</sub> products. These developments provide valuable insights into sustainable carbon utilization and the design of advanced catalytic materials for high-performance applications.

### 3.1 Photothermal catalytic reduction of CO<sub>2</sub> to C<sub>1</sub> products

H<sub>2</sub> and CH<sub>4</sub> are primary reductants used in the reduction of CO<sub>2</sub>, which correspond to hydrogenation and reforming.<sup>107</sup> The following will provide an overview of the main reactions of catalytic reduction of CO<sub>2</sub> to C<sub>1</sub> products.

**3.1.1 Reverse water-gas shift reaction.** The reverse water-gas shift (RWGS) reaction involves the interaction of CO<sub>2</sub> and H<sub>2</sub> to produce CO and H<sub>2</sub>O. This reaction serves as a key pathway for converting CO<sub>2</sub> into high-value chemicals. The resulting synthesis gas (CO and H<sub>2</sub>O) can then be utilized in downstream processes, such as the Fischer-Tropsch reaction, to produce alcohols and other hydrocarbons.

However, RWGS is an endothermic reaction that requires high temperature conditions to proceed favorably, and the process consumes a lot of energy.<sup>108,109</sup> RWGS reactions are thermodynamically favorable at high temperature, but can lead to carbon formation and unwanted byproducts. At the same time, too high temperature also faces the risk of metal sintering and coke deposition leading to catalyst deactivation.<sup>110</sup> At lower temperatures (below 500 °C), the reaction is kinetically unfavorable, necessitating extensive catalyst use. Therefore, current research focuses on developing different catalytic systems in photothermal catalytic processes and exploring milder catalytic conditions.

Research on metal catalysts is primarily focused on those based on Ni, Co, Cu, Fe, and Mo nanoparticles (NPs). Liu *et al.*<sup>111</sup> developed a catalyst consisting of Co NPs with N-doped carbon, created through a two-step pyrolysis of a ZIF-67 precursor (Fig. 11a). Their Co@NC-700 catalyst demonstrated high activity and selectivity for the photocatalytic hydrogenation of CO<sub>2</sub> to CO, achieving a CO generation rate of 0.75 mol g<sub>cat</sub><sup>-1</sup> h<sup>-1</sup> and a CO selectivity of 92.6% under full-spectrum light. The exceptional performance was due to the synergistic effects of the well-coordinated Co NPs, carbon layer thickness, and N-doping species. The catalyst's durability is enhanced by carbon encapsulation, providing a simple and effective approach to producing highly active and long-lasting non-noble metal catalysts.

Yan and co-workers discovered that nanostructured BiOBr semiconductor catalyst, with its staggered layered structure, was a promising photocatalyst.<sup>112</sup> They found frustrated Lewis pairs on the surface of BiOBr, serving as effective catalytic sites for CO<sub>2</sub> reduction. Meanwhile, introducing Ce<sup>4+</sup> and oxygen vacancies (Fig. 11b) optimized the electronic state and FLP properties, forming frustrated Lewis acid-base pairs that significantly enhance the CO<sub>2</sub> reduction to CO. This work offers a strategy for constructing efficient photocatalysts and understanding the atomic-level mechanisms of photocatalysis.

The use of noble metals entails a significant cost. In order to reduce the price of the catalysts, non-noble transition metals have also been studied as part of catalysts in photothermal-catalytic reactions as a more economical option. Ning *et al.* synthesized a hybrid carbon-based catalyst with embedded Co NPs together with dispersed Co-N species, denoted as Co@CoN&C.<sup>113</sup> The reactions were carried out at 55 kPa, using an equal amount of CO<sub>2</sub> and H<sub>2</sub> and a Xe lamp in a batch



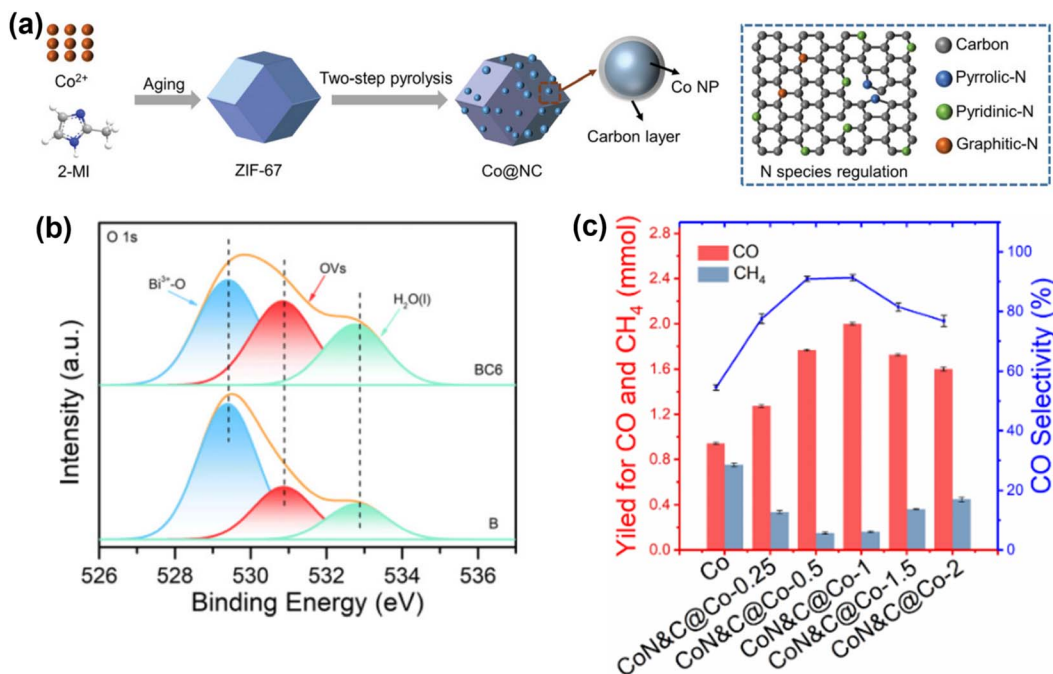


Fig. 11 (a) Schematic illustration for the preparation of N-doped carbon-coated Co NPs.<sup>111</sup> Copyright 2023, Wiley. (b) High-resolution XPS spectra of O 1s for BiOBr and BC6.<sup>112</sup> Copyright 2022, American Chemical Society. (c) Time course of CO and CH<sub>4</sub> yield within 30 min and product selectivity for CO<sub>2</sub> hydrogenation over Co and Co@CoN&C under irradiation.<sup>113</sup> Copyright 2020, American Chemical Society.

reactor. Initially, the photoinduced thermal-effect was demonstrated as evidenced by the increase of temperature of the catalyst surface during the reaction, which reached 518 °C, while the plain Co NP system increased only up to 300 °C. After 30 min of irradiation, the optimized showed 41% CO<sub>2</sub> conversion and a CO selectivity of 91% (132 mmol CO g<sup>-1</sup> h<sup>-1</sup>), meanwhile the unsupported Co NPs showed 43% CO selectivity (Fig. 11c). The high reaction rate of the hybrid catalyst was attributed to the significant photo-thermal effect, and the CO selectivity was improved by the special characteristics provided by the Co-N shell in comparison with plain Co NPs.

**3.1.2 CO<sub>2</sub> dry reforming of methane reaction.** The dry reforming of CH<sub>4</sub> (DRM) [eqn (14)] converts CH<sub>4</sub> and CO<sub>2</sub> into syngas, a valuable feedstock gas consisting of H<sub>2</sub> and CO.<sup>114,115</sup> Due to the endothermic nature of DRM reactions, high temperatures and large energy inputs are required which can lead to CH<sub>4</sub> decomposition and carbon deposition. Additionally, side reactions like the RWGS reaction can occur, impeding the desired process. Therefore, addressing carbon deposition in CH<sub>4</sub> dry reforming and conducting photocatalytic reactions under mild conditions are current research focal points.



It has been reported that integrating photothermal and photoelectric catalytic processes could achieve a redox cycle that promotes metal-to-metal charge transfer induced by light, enabling low-temperature DRM. Ma *et al.*<sup>116</sup> demonstrated that the redox cycle photocatalyst Rh/Ce<sub>x</sub>WO<sub>3</sub> (Fig. 12a-c) ensured the stability and anti-coking performance of light-driven DRM

without external heating. The photothermal and photoelectric effects play a key role in light-driven DRM, surpassing thermodynamic limitations. Calculations indicated that the strong CO<sub>2</sub> absorption of Ce<sub>x</sub>WO<sub>3</sub>, its high oxygen mobility, and the oxygen bridge reduce the initiation temperature of DRM. This advancement paves the way for developing low-temperature catalysts for DRM.

Recently, Tang and colleagues reported a photothermal catalyst Ru/SrTiO<sub>3</sub> under 600 °C and 300 W xenon lamp irradiation, the yields of CO and H<sub>2</sub> were 1.4–1.5 times higher than those achieved with the thermal catalytic method.<sup>117</sup> In the Ru/SrTiO<sub>3</sub> catalyst (Fig. 12d), light induced the transfer of electrons from SrTiO<sub>3</sub> to Ru, which participated in CH<sub>4</sub> dehydrogenation and H<sub>2</sub> production, thereby reducing the reaction energy barrier. This study elucidated the mechanism of photothermal DRM, providing valuable guidance for the future solar photothermal conversion of greenhouse gases.

Among various CH<sub>4</sub> activation reactions, methane coupling is a promising potential pathway for directly obtaining valuable C<sub>2+</sub> hydrocarbons. Long *et al.*<sup>23</sup> proposed an innovative structure, the single-atom nest, to enhance the performance of photochemical non-oxidative coupling of methane (NOCM). Pt single-atom nests were fabricated as proof-of-concept single-atom nest photocatalysts. The results showed that Pt single-atom nests led to a remarkable 3.2-fold enhancement in the photocatalytic C<sub>2</sub>H<sub>6</sub> yield under simulated sunlight, compared to Pt single-atoms. This work presents a pioneering concept for improving the efficiency of coupling reactions.

**3.1.3 Methanation reaction.** CH<sub>4</sub> is a primary product of the hydrogenation reduction of CO<sub>2</sub>, also known as the Sabatier

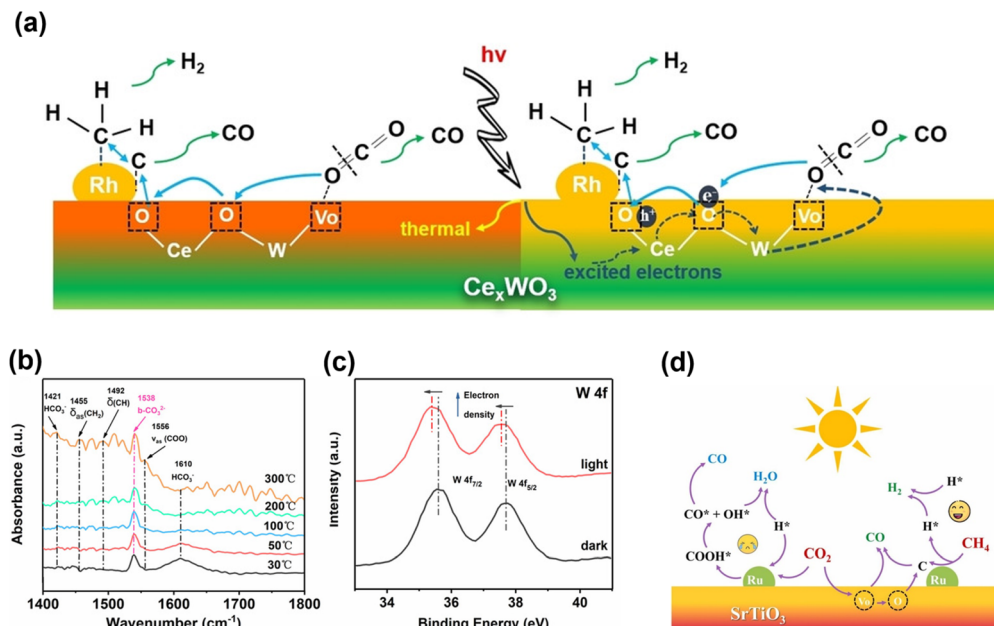


Fig. 12 (a) Schematic diagram for light-driven DRM reaction over Rh/Ce<sub>x</sub>WO<sub>3</sub> catalyst. (b) *In situ* DRIFT spectra of Rh/Ce<sub>x</sub>WO<sub>3</sub> measured in CH<sub>4</sub>/CO<sub>2</sub> mixture under different temperature. (c) ISI-XPS spectra of W 4f of Rh/Ce<sub>x</sub>WO<sub>3</sub> with and without illumination.<sup>116</sup> Copyright 2022, Wiley. (d) Schematic diagram of the photothermal DRM reaction over the Ru/SrTiO<sub>3</sub> catalyst. Adapted with permission from ref. 117 Copyright 2023, Elsevier.

reaction. This exothermic reaction is thermodynamically favorable at lower temperatures. Among the many catalysts developed for this reaction, Ru-based catalysts are considered the best for low-temperature methanation. Although Ni-based catalysts are much cheaper than Rh and Ru-based catalysts, they are prone to deactivation due to carbon deposition. Ru is scarce and expensive, but Ru-loaded catalysts can effectively catalyze CO<sub>2</sub> hydrogenation under a wide range of operating conditions. Meanwhile, metal oxides such as TiO<sub>2</sub>, Al<sub>2</sub>O<sub>3</sub>, CeO<sub>2</sub>, and ZrO<sub>2</sub> are widely used as support materials.

Metal-organic frameworks (MOFs) are considered to be ideal carriers for active metal NPs. MOF-encapsulated metal NPs, due to the porous nature of MOFs, prevent sintering and aggregation of the metal NPs and facilitate the smooth diffusion of reactants and products within the nanochannels. Wang *et al.*<sup>118</sup> successfully encapsulated Ir NPs of approximately 1.5 nm into UiO-66 (Fig. 13a), forming Ir@UiO-66. The Ir NPs effectively promoted the separation and transfer of photo-induced charge carriers in the excited UiO-66, thereby aiding the cleavage of H<sub>2</sub> and the activation of CO<sub>2</sub>. Under light irradiation, Ir@UiO-66-2 showed an excellent CH<sub>4</sub> yield of 19.9 mmol g<sub>cat</sub><sup>-1</sup> h<sup>-1</sup> and high selectivity (95%) at 250 °C. This study offers a new strategy for designing CO<sub>2</sub> methanation catalysts under mild conditions.

Solar-driven reactions are increasingly being considered to address the poor thermal catalytic performance of low-temperature methanation. These reactions are expected to reduce the excessive energy consumption of traditional thermal catalytic methods while extending the catalyst's lifespan. Zhou *et al.*<sup>119</sup> designed a TiO<sub>2</sub> photocatalyst loaded with Ru NPs (Fig. 13b), significantly improving the conversion efficiency of

CO<sub>2</sub> to CH<sub>4</sub> under light irradiation. The photo-induced electrons transfer effectively promoted the dissociation of H<sub>2</sub> and the activation of CO<sub>2</sub> on Ru atoms. This work provides new theoretical insights into the activation and methanation of CO<sub>2</sub> under light irradiation.

**3.1.4 CH<sub>3</sub>OH synthesis.** CH<sub>3</sub>OH is an important industrial chemical, making the reduction of CO<sub>2</sub> to CH<sub>3</sub>OH a promising strategy for CO<sub>2</sub> conversion. This exothermic reaction is favorable at low temperatures and high pressures, which increase CH<sub>3</sub>OH yield. Although Cu-based catalysts exhibit high activity, they suffer from low selectivity for CH<sub>3</sub>OH due to competing RWGS reactions and deactivation through sintering of Cu.

It has been reported that the combination of two component catalysts is an effective way to improve catalytic activity: a metal oxide for CO<sub>2</sub> activation and a metal or reducible metal oxide for H<sub>2</sub> activation. Li *et al.*<sup>120</sup> have developed a novel Cd/TiO<sub>2</sub> catalyst (Fig. 13c), which exhibited a CH<sub>3</sub>OH selectivity of 81%, a CO<sub>2</sub> conversion rate of 15.8%, and a CH<sub>4</sub> selectivity of less than 0.7%. Experimental and computational studies indicated that the unique electronic properties of Cd clusters supported by the TiO<sub>2</sub> matrix were responsible for the high selectivity of hydrogenating CO<sub>2</sub> to CH<sub>3</sub>OH *via* the HCOO\* pathway at the interfacial catalytic sites.

This discovery underscores the significance of the synergistic action between the two components of the catalyst: the metal oxide facilitates CO<sub>2</sub> activation and transformation, while the metal or reducible metal oxide promotes H<sub>2</sub> activation and dissociation. This finding highlights the importance of material design and understanding the underlying mechanisms in catalysis.



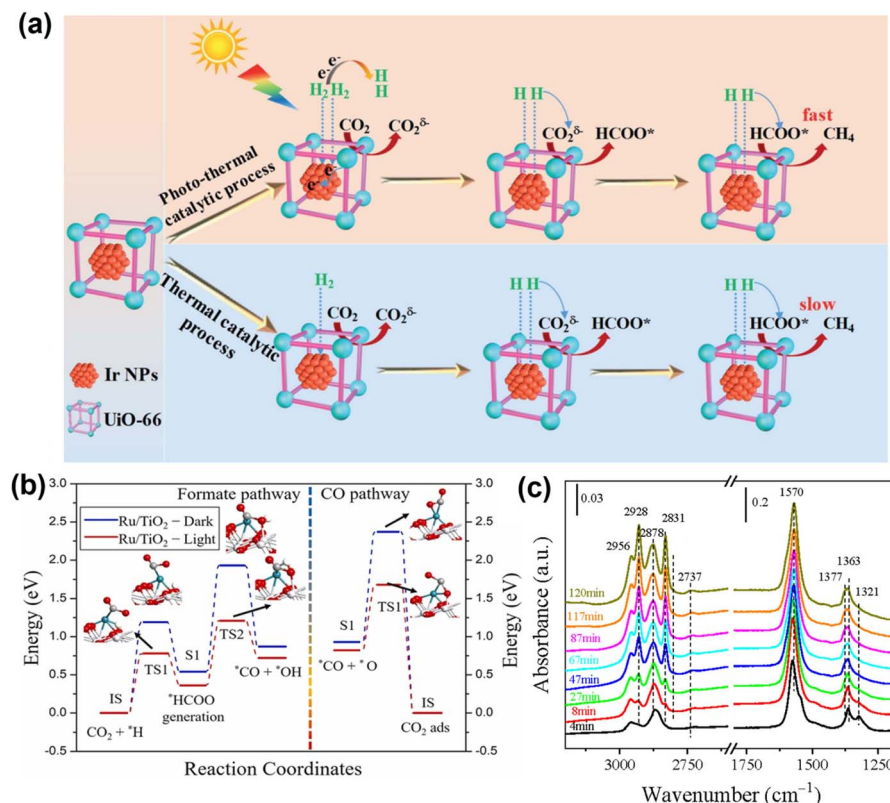


Fig. 13 (a) Proposed reaction mechanism for the thermal and photo-thermal catalytic Sabatier reaction process over Ir@UiO-66.<sup>118</sup> Copyright 2022, Royal Society of Chemistry. (b) Feasible routes of the CO<sub>2</sub> hydrogenation reaction on the Ru/TiO<sub>2</sub> model surface under dark and light conditions.<sup>119</sup> Copyright 2022, Elsevier. (c) *In situ* DRIFT spectra obtained from the surface species formed during the reaction for 3.5% Cd/TiO<sub>2</sub>.<sup>120</sup> Copyright 2022, Elesvier.

### 3.2 C<sub>2-4</sub> hydrocarbons

In addition to producing CO, CH<sub>4</sub>, CH<sub>3</sub>OH, and other C<sub>1</sub> products, CO<sub>2</sub> reduction can also yield multi-carbon hydrocarbons (C<sub>2-4</sub>) with broader applications. The production of C<sub>2-4</sub> compounds can be achieved through methods such as petroleum refining, direct or indirect conversion of synthesis gas, or CO<sub>2</sub> hydrogenation. This process addresses environmental issues like the “greenhouse effect” resulting from rising CO<sub>2</sub> concentrations. Therefore, the photocatalytic or photo-thermal catalytic conversion of CO<sub>2</sub> into C<sub>2-4</sub> products is an effective approach for mitigating energy shortages. The conversion from C<sub>1</sub> products to multi-carbon products requires a C–C coupling reaction. Currently, there are two main methods to achieve this: (1) the Fischer–Tropsch process, where CO<sub>2</sub> is first converted into CO through the reverse water-gas shift reaction and then into C<sub>2-4</sub> via the Fischer–Tropsch process;<sup>121</sup> (2) the CH<sub>3</sub>OH process, where CO<sub>2</sub> is hydrogenated to produce CH<sub>3</sub>OH, which is then converted into C<sub>2-4</sub> through the methanol-to-hydrocarbons process. These methods represent important steps in developing sustainable and efficient technologies for CO<sub>2</sub> conversion.<sup>122</sup>

**3.2.1 Photocatalytic CO<sub>2</sub> reduction to C<sub>2-4</sub> hydrocarbons.** Photocatalysis is a crucial approach to achieving sustainable production of green energy by converting solar energy into chemical energy through semiconductor materials under

ultraviolet and visible light. Yan and cooperators reported the advantages of heterojunction and reduced graphene oxide (rGO) and proposed that the combination of In<sub>2</sub>S<sub>3</sub>/In<sub>2</sub>O<sub>3</sub> heterojunctions and rGO could further enhance electron transfer, thereby improving CO<sub>2</sub> conversion (Fig. 14b),<sup>124</sup> with the total selectivity of C<sub>2+</sub> reaching about 35%. Additionally, Yan *et al.*<sup>123</sup> developed a metal–organic framework Prussian blue with excellent light absorption ability, loaded with NiFe, exhibited excellent photocatalytic performance, with a CO<sub>2</sub> conversion rate of 34.7% and a C<sub>2-4</sub> selectivity of 33.6% (Fig. 14a and c). Xiong *et al.*<sup>125</sup> reported a unique Cu-Ti-VO/Ti<sub>0.91</sub>O<sub>2</sub>-SL photocatalyst for highly efficient and selective conversion of CO<sub>2</sub> into C<sub>3</sub>H<sub>8</sub> (Fig. 14d–f).

**3.2.2 Photothermal catalytic CO<sub>2</sub> hydrogenation to C<sub>2-4</sub> hydrocarbons.** Research findings indicate that the yield of photocatalytic CO<sub>2</sub> hydrogenation is relatively low, but introducing thermal energy into the photocatalytic reaction can effectively improve CO<sub>2</sub> hydrogenation performance. Photothermal catalysis convert light to increase the surface temperature of a catalyst, initiating a thermal catalytic reaction and converting light energy into chemical energy. This approach is highly promising for CO<sub>2</sub> reduction, as it utilizes the extensive absorption of solar spectra to combine thermochemical and photochemical processes, synergistically promoting catalytic reactions and achieving efficient CO<sub>2</sub> conversion under



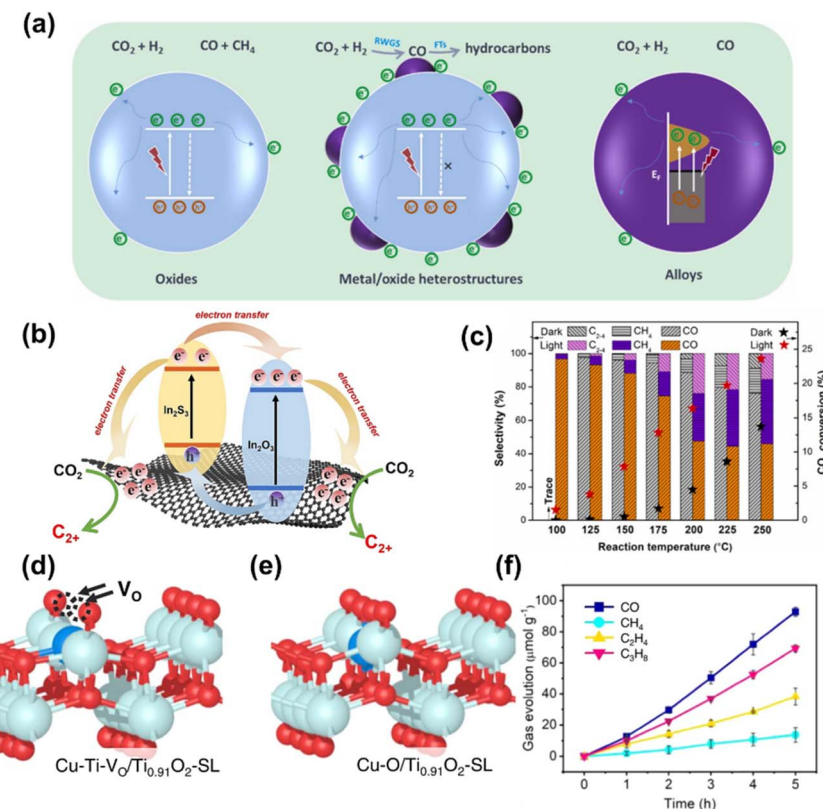


Fig. 14 (a) The proposed photocatalytic CO<sub>2</sub> hydrogenation mechanism on NiFe-x alloys catalysts.<sup>123</sup> Copyright 2022, Elsevier BV. (b) Schematic diagram of the multiple channels for electrons and holes transfer between In<sub>2</sub>O<sub>3</sub>, In<sub>2</sub>S<sub>3</sub> and rGO.<sup>124</sup> Copyright 2023, Elsevier. (c) Product selectivity and CO<sub>2</sub> conversion at different reaction temperatures over NiFe-300 catalyst.<sup>123</sup> Copyright 2022, Elsevier BV. (d and e) The atomic structure configuration (colour codes: light blue (Ti), blue (Cu), and red (O)). (f) Photocatalytic product evolution as a function of light irradiation times on Cu-Ti-V<sub>O</sub>/Ti<sub>0.91</sub>O<sub>2</sub>-SL.<sup>125</sup> Copyright 2023, Springer Nature.

relatively mild conditions. While photocatalysis offers mild reaction conditions and precise reaction control, it suffers from slow reaction rates and the need for long-term illumination. Photothermal catalysis addresses these issues by offering improved reaction rates, good selectivity of reaction products, and stability of thermosensitive catalysts.

Zhang and co-workers<sup>126</sup> successfully prepared a series of new Fe-based catalysts with different chemical compositions using FeMgAl-LDH catalysts through hydrogen reduction at temperatures from 300 °C to 700 °C, of which catalyst obtained by hydrogen reduction at 500 °C (Fe-500) demonstrated excellent CO<sub>2</sub> hydrogenation capabilities (Fig. 15a). These high-performance Fe-based catalysts were used for photothermal CO<sub>2</sub> hydrogenation to C<sub>2+</sub> hydrocarbons at atmospheric pressure. The FeO nanoparticles and FeO<sub>x</sub> loaded on MgO-Al<sub>2</sub>O<sub>3</sub> showed a CO<sub>2</sub> conversion rate of 50.1%, C<sub>2+</sub> selectivity of 52.9%, and excellent stability over 22 hours of continuous testing (Fig. 15b). Zhang *et al.*<sup>52</sup> also developed novel CoFe-based catalysts, using layered-double-hydroxide (LDH) nanosheets for hydrogen reduction to generate C<sub>2+</sub> hydrocarbons. The CoFe-650 catalyst demonstrated remarkable selectivity toward hydrocarbons, with 60% CH<sub>4</sub> and 35% C<sub>2+</sub> (Fig. 15c). Additionally, Zhang *et al.*<sup>127</sup> reported a hydrophobic core-shell Fe-based FTS catalyst, Fe/Fe<sub>3</sub>C-c, prepared by a three-step process

including hydrothermal synthesis, thermal decomposition, and hydrophobic modification (Fig. 15d). The optimized Fe/Fe<sub>3</sub>C-c catalyst, driven by light irradiation, delivered attractive light-olefins selectivities of 48.0% with an O/P ratio of 10.1 for batch-type reactions and 49.0% with an O/P ratio of 12.2 for flow-type reactions (Fig. 15e).

Yan and colleagues<sup>128</sup> synthesized graphdiyne/In<sub>2</sub>O<sub>3</sub> (GDY-IO) nanocomposites for gas-phase photocatalytic CO<sub>2</sub> reduction to C<sub>2+</sub> hydrocarbons. By adjusting the composite ratio of GDY and In<sub>2</sub>O<sub>3</sub>, the 0.4% GDY-IO catalyst exhibited optimal C<sub>2+</sub> hydrocarbons production activity and a high selectivity of 14% under simulated solar light irradiation and atmospheric pressure (Fig. 16a, b). Ozin *et al.*<sup>129</sup> reported that cobalt ferrite (CoFe<sub>2</sub>O<sub>4</sub>) spinel produced C<sub>2-4</sub> hydrocarbons in a single-step, ambient-pressure photocatalytic hydrogenation of CO<sub>2</sub>, with a rate of 1.1 mmol g<sup>-1</sup> h<sup>-1</sup>, a selectivity of 29.8%, and a conversion yield of 12.9%. The CoFe<sub>2</sub>O<sub>4</sub> reconstructed into a CoFe-CoFe<sub>2</sub>O<sub>4</sub> alloy-spinel nanocomposite, facilitating the light-assisted transformation of CO<sub>2</sub> to CO and subsequent hydrogenation to C<sub>2-4</sub> hydrocarbons (Fig. 16c and d).

Corma *et al.*<sup>130</sup> investigated the CO<sub>2</sub> hydrogenation into hydrocarbons promoted by sunlight on Co nanoparticles covered by thin carbon layers. They achieved nearly 100% selectivity to hydrocarbons, with increased selectivity towards



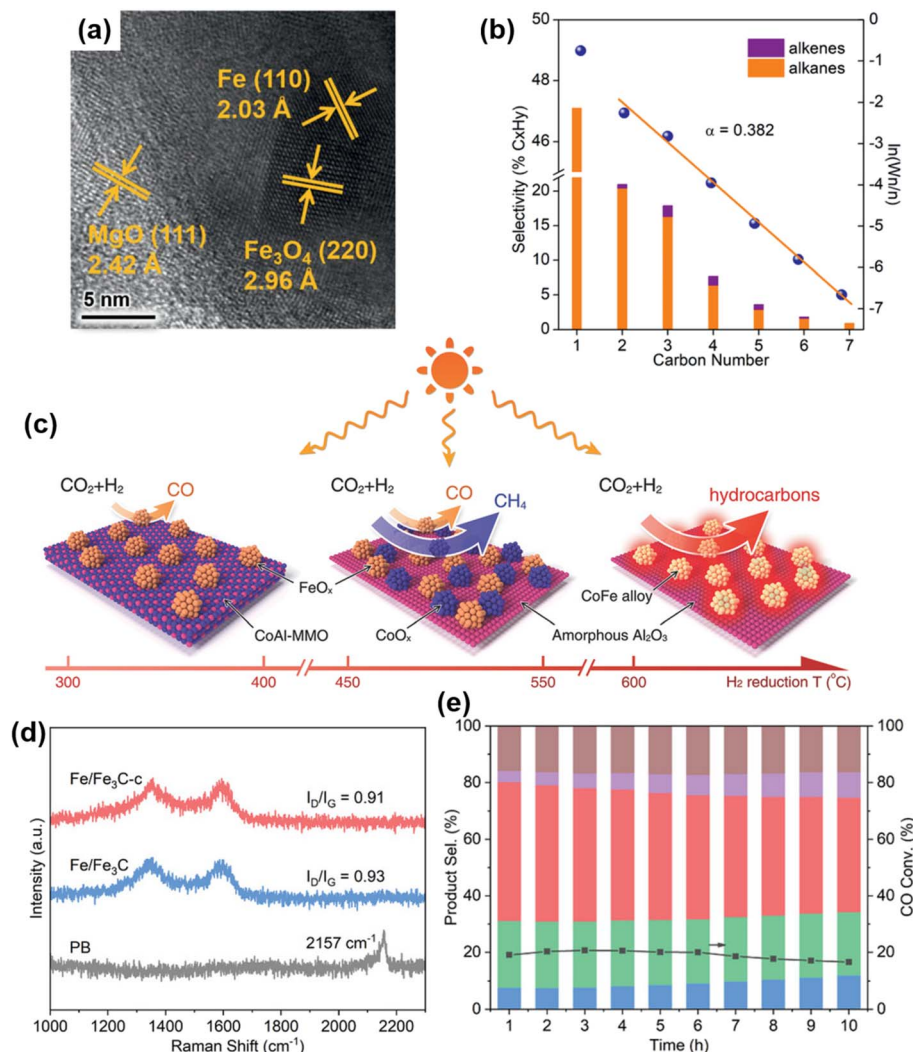


Fig. 15 (a) HRTEM image of Fe-500. (b) The hydrocarbon product distribution obtained over Fe-500 under UV-vis irradiation.<sup>126</sup> Copyright 2021, Wiley. (c) Illustration of the different CoFe-x catalysts formed by hydrogen reduction of a CoFeAl-LDH nanosheet precursor at different temperatures. The CO<sub>2</sub> hydrogenation selectivity of each CoFe-x catalyst is indicated.<sup>52</sup> Copyright 2018, Wiley. (d) Raman spectra of PB, Fe/Fe<sub>3</sub>C and Fe/Fe<sub>3</sub>C-c catalysts. (e) The FTS performance of the Fe/Fe<sub>3</sub>C-c catalyst in a flow system (1 ML min<sup>-1</sup>).<sup>127</sup> Copyright 2024, Wiley-VCH Verlag.

C<sub>2+</sub> hydrocarbons and alcohols (mainly ethanol) using Na-promoted Co nanoparticles (Na-Co@C) (Fig. 17a and b). Furthermore, Corma *et al.*<sup>131</sup> prepared nickel-iron oxide nanoparticles by decomposing a mixed oxalate precursor and used them as catalysts for sunlight-promoted CO<sub>2</sub> hydrogenation (Fig. 17c and d). The intimate contact between crystalline NiO and  $\gamma$ -Fe<sub>2</sub>O<sub>3</sub> (and possibly amorphous iron oxide) domains in NiFeO<sub>x</sub>, NiFe<sub>3</sub>O<sub>x</sub>, and NiFe<sub>9</sub>O<sub>x</sub> proved highly efficient for generating light alkanes, which can be used as synthetic fuels.

Amin *et al.*<sup>132</sup> prepared Ag-loaded TiO<sub>2</sub> nanoparticles with varying Ag concentrations using an improved sol-gel method and fixed them on a monolithic support. The Ag/TiO<sub>2</sub> catalyst demonstrated significant photocatalytic activity for the dynamic reduction of CO<sub>2</sub> to CO *via* the RWGS reaction in both continuous cell and integrated photoreactors. Compared to battery-type photoreactors, integrated photoreactors effectively converted CO<sub>2</sub> into CO as the main product through Ag/TiO<sub>2</sub>, while also producing multi-carbon products like C<sub>2-4</sub>.

Building on this progress, we constructed a C-C coupling center for C<sub>1</sub> intermediates *via* the *in situ* formation of Co<sup>0</sup>-Co<sup>δ+</sup> interface double sites on MgAl<sub>2</sub>O<sub>4</sub> (Co-CoO<sub>x</sub>/MAO) (Fig. 17e).<sup>9</sup> The Co-CoO<sub>x</sub>/MAO exhibited a high C<sub>2-4</sub> hydrocarbons production rate of 1303  $\mu\text{mol g}^{-1} \text{h}^{-1}$ , with a total organic carbon selectivity of 62.5% for C<sub>2-4</sub> hydrocarbons under light irradiation and a high olefin to paraffin ratio ( $\approx 11$ ), demonstrating its efficiency and selectivity for multi-carbon hydrocarbon production. Future research could focus on optimizing catalyst compositions, enhancing light absorption, and improving reaction kinetics to further increase the yield and selectivity of C<sub>2+</sub> products.

### 3.3 C<sub>4+</sub> hydrocarbons

Despite successful reports on the hydrogenation of CO<sub>2</sub> to produce value-added C<sub>2+</sub> chemicals, synthesizing C<sub>4+</sub> remains a significant challenge due to the high barrier of C-C coupling. C<sub>5+</sub> hydrocarbons (liquid gasoline), which contain five or more

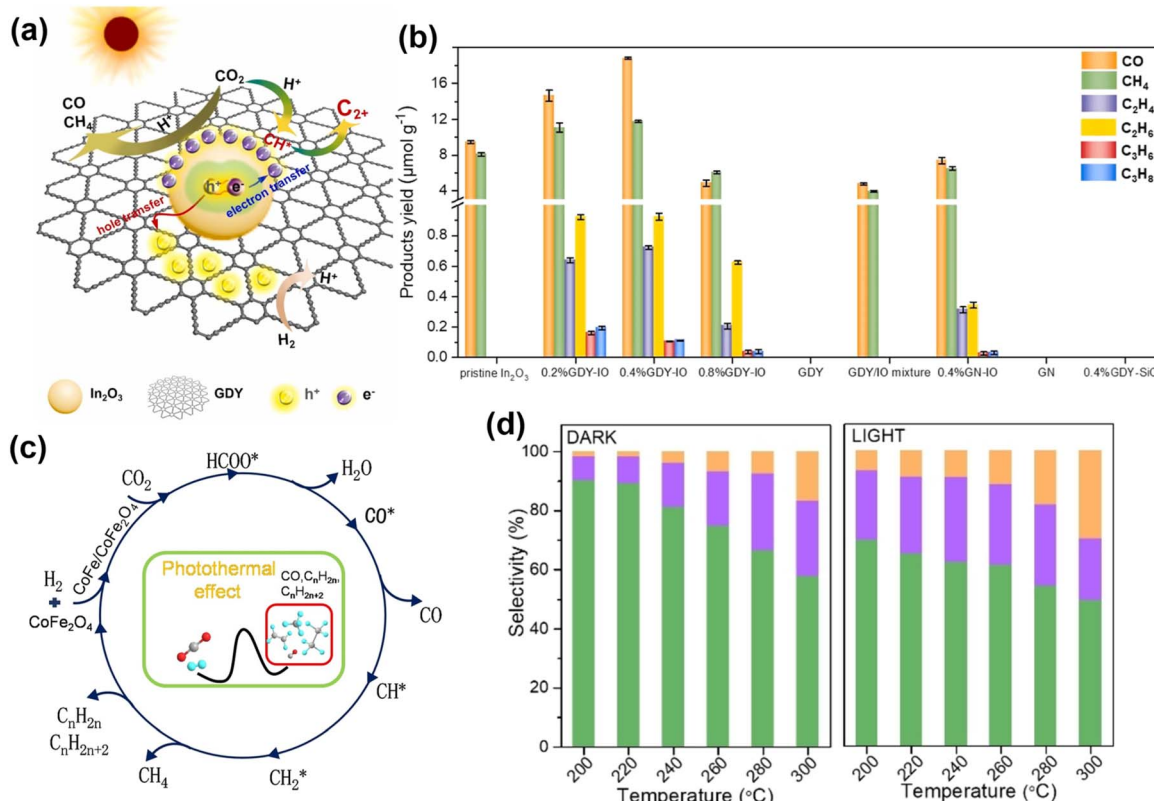


Fig. 16 (a) The charge carrier separation pathways and photocatalytic mechanism for  $\text{CO}_2$  hydrogenation over graphdiyne-modified  $\text{In}_2\text{O}_3$  composite. (b) Products of photocatalytic  $\text{CO}_2$  reduction on various catalysts.<sup>128</sup> Copyright 2024, Elsevier. (c) Possible reaction pathway of  $\text{FC}_2$  for  $\text{CO}_2$  hydrogenation. (d) The corresponding selectivity of  $\text{CO}$ ,  $\text{CH}_4$ , and  $\text{C}_{2-4}$  hydrocarbons for sample  $\text{FC}_2$  with and without light irradiation in the temperature range of 200–300 °C and atmospheric press.<sup>129</sup> Copyright 2023, Wiley.

carbon atoms, are important products in the petrochemical industry. In photocatalytic  $\text{CO}_2$  hydrogenation reactions, generating  $\text{C}_{5+}$  products faces higher energy barriers due to the C–C coupling reaction. There has not yet been a decisive study on the production of liquid gasoline from  $\text{CO}_2$  hydrogenation.

Zhang *et al.*<sup>52</sup> developed an  $\text{Al}_2\text{O}_3$ -supported CoFe alloy catalyst, adjusting its surface chemical composition by changing the reduction temperature of the CoFeAl-LDH nanosheet precursor, thereby optimizing the activity and product selectivity of  $\text{CO}_2$  hydrogenation (Fig. 15c). The CoFe-650 catalyst achieved efficient hydrogenation of  $\text{CO}_2$  to  $\text{C}_{4+}$  with a selectivity of 8.3% under photothermal conditions, demonstrating the potential for using solar energy to produce high-value chemicals. Subsequently, Zhang *et al.* prepared a series of novel Fe-based catalysts with varying chemical compositions by reducing MgFeAl layered double hydroxide nanosheets at temperatures ranging from 300 °C to 700 °C.<sup>126</sup> Using a 300 W xenon lamp as the light source, the Fe-500 catalyst showed excellent stability for  $\text{C}_{2+}$  hydrocarbons under UV-visible light irradiation over 22 hours of continuous testing, with a  $\text{C}_{5+}$  selectivity of 6.3% (Fig. 18b), maintaining its activity and selectivity without significant deactivation. Ma and his research team<sup>133</sup> developed a K-promoted  $\text{Ru/Fe}_3\text{O}_4$  catalyst, achieving the production of high-value chemicals and fuels through photocatalytic  $\text{CO}_2$  hydrogenation (Fig. 18a). When using the K-

$\text{Ru/Fe}_3\text{O}_4$  catalyst for  $\text{CO}_2$  hydrogenation, the selectivity of  $\text{C}_{5+}$  reached 19.0%, indicating that the introduction of a potassium promoter can enhance C–C coupling, thereby improving the yield of  $\text{C}_{5+}$  products. Yan *et al.*<sup>134</sup> incorporated magnetic cobalt ions into ultra-thin  $\text{BiOCl}$  sheets to achieve selective control of the photocatalytic  $\text{CO}_2$  reduction reaction. Co- $\text{BiOCl}$  can selectively convert  $\text{CO}_2$  into  $\text{CH}_4$  and  $\text{C}_{2+}$  products, with a hydrocarbon selectivity of up to 76.9%, a performance not possessed by the original  $\text{BiOCl}$  (Fig. 18c). These results were significant for improving the efficiency of converting  $\text{CO}_2$  into high-value chemicals and demonstrates the potential of photocatalytic technology to convert  $\text{CO}_2$  into useful chemicals under mild conditions. Under light conditions, electron transfer on the catalyst surface can change the adsorption/desorption dynamics of reaction intermediates, affecting the reaction path and making the distribution of  $\text{C}_{5+}$  products significantly different from the thermal catalysis process, providing a new strategy for solar-driven  $\text{CO}_2$  conversion.

Song *et al.*<sup>135</sup> highlighted the dynamic evolution of active iron and carbon species in  $\text{CO}_2$  hydrogenation over Fe-Zr catalysts supported on different zirconia forms (monoclinic  $\text{m-ZrO}_2$  and tetragonal  $\text{t-ZrO}_2$ ). During CO pre-reduction, the  $\text{FeO}$  intermediate species on the Fe-K/m-ZrO<sub>2</sub> catalyst indicated mild and sufficient reduction of  $\text{Fe}_2\text{O}_3$  on  $\text{m-ZrO}_2$  (Fig. 19a), promoting the carbonization reaction to form smaller and more active iron



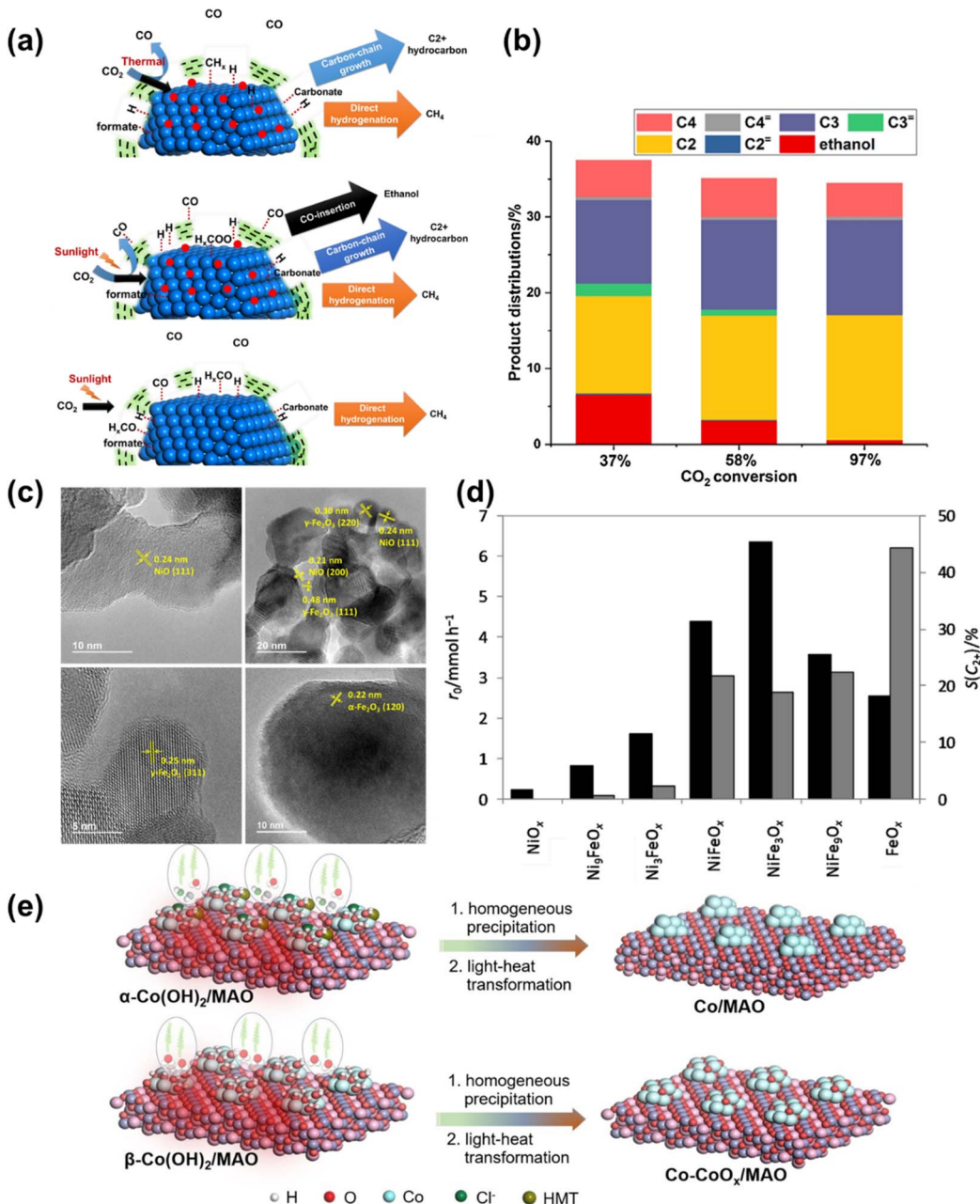


**Fig. 17** (a) Schematic illustration of the CO<sub>2</sub> hydrogenation on Na-Co@C and Co@C catalysts under thermal and photothermal conditions. Sodium is shown with red circles. (b) Selectivity to C<sub>2+</sub> hydrocarbons and ethanol under photothermal conditions at different CO<sub>2</sub> conversion.<sup>130</sup> Copyright 2018, Elsevier. (c) HRTEM micrographs (200 kV) of Ni<sub>1-x</sub>Fe<sub>x</sub>O<sub>x</sub> materials: Ni<sub>9</sub>FeO<sub>x</sub>, Ni<sub>3</sub>FeO<sub>x</sub>, NiFe<sub>9</sub>O<sub>x</sub>, and FeO<sub>x</sub>. (d) Initial CO<sub>2</sub> conversion rate ( $r_0$ , black bars) and hydrocarbon selectivity towards C<sub>2+</sub> products [ $S(C_{2+})$ , excluding CO, grey bars] obtained from CO<sub>2</sub> hydrogenation experiments on the series of Ni<sub>1-x</sub>Fe<sub>x</sub>O<sub>x</sub> materials.<sup>131</sup> Copyright 2018, Springer. (e) A schematic illustration of the two-step growth of  $\alpha$ - and  $\beta$ -Co(OH)<sub>2</sub> nanosheets on MAO and light-to-heat reduction.<sup>9</sup> Copyright 2023, Wiley.

species (Fe<sub>3</sub>O<sub>4</sub> and  $\chi$ -Fe<sub>5</sub>C<sub>2</sub>). When the Fe content reached 15 wt%, the Fe-K/m-ZrO<sub>2</sub> catalyst showed a significant CO<sub>2</sub> conversion rate (38.8%) and light olefins selectivity (42.8%). Jing *et al.*<sup>129</sup> reported a photocatalyst, cobalt ferrite (CoFe<sub>2</sub>O<sub>4</sub>), which converts CO<sub>2</sub> into C<sub>2-4</sub> hydrocarbons through a photo-thermal catalytic process at ambient pressure and temperature (Fig. 19b). The active sites are formed by the transformation of CoFe<sub>2</sub>O<sub>4</sub> into a nano-composite of CoFe alloy and CoFe<sub>2</sub>O<sub>4</sub>, synergistically promoting the conversion of CO<sub>2</sub> to CO and

subsequent CO hydrogenation, effectively producing C<sub>2-4</sub> hydrocarbons. A 35 hours stability test under atmospheric pressure and light exposure showed this sample continuously producing C<sub>2-4</sub> hydrocarbons, along with CO and CH<sub>4</sub>, achieving a C<sub>2-4</sub> hydrocarbons selectivity of 29.8% and a high CO<sub>2</sub> conversion efficiency (12.9%) (Fig. 19c). Mechanism studies showed CO<sub>2</sub> was first adsorbed on the CoFe<sub>2</sub>O<sub>4</sub> surface, then converted into formate intermediates under hydrogen action. These intermediates further hydrogenated to produce

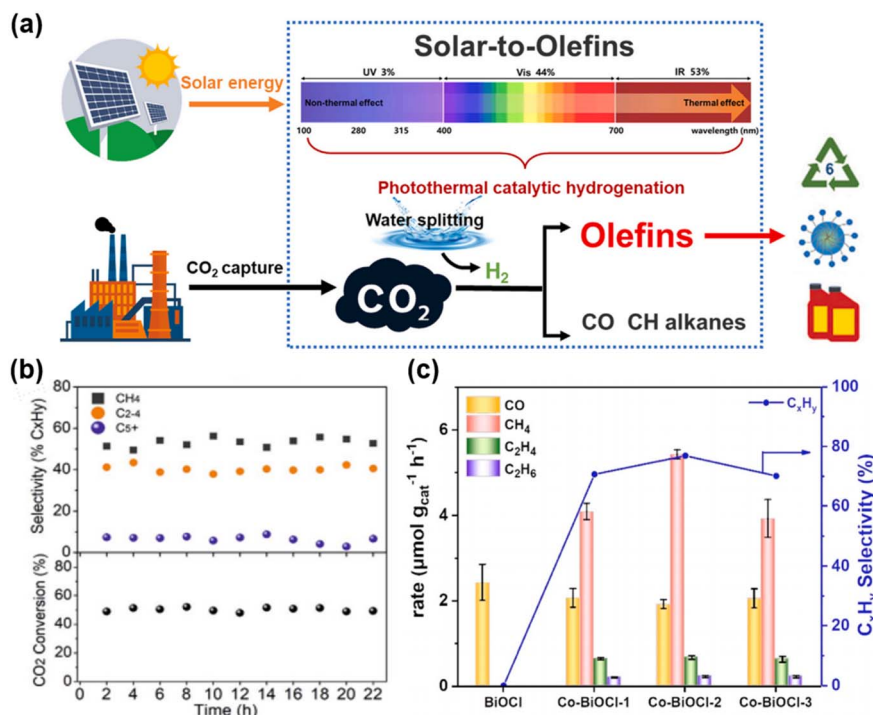


Fig. 18 (a) Photodriven hydrogenation of  $\text{CO}_2$  to lower olefins, which can be efficiently performed in a photothermally catalytic way with the  $\text{K}-\text{Ru}/\text{Fe}_3\text{O}_4$  catalyst presented in this work.<sup>133</sup> Copyright 2024, Cell Press. (b) The  $\text{CO}_2$  conversion and product selectivities over Fe-500 under UV-vis irradiation using a flow system with a flow rate of  $5 \text{ mL min}^{-1}$ .<sup>126</sup> Copyright 2021, Wiley. (c) Photocatalytic  $\text{CO}_2$  hydrogenation activity and selectivity of  $\text{C}_x\text{H}_y$  on Co–BiOCl with different Co content after 4 h light irradiation of  $\text{C}_x\text{H}_y$  on Fe–BiOCl, Cu–BiOCl, Ni–BiOCl and Zn–BiOCl.<sup>134</sup> Copyright 2024, Elsevier.

CO and water through the RWGS reaction, with CO further hydrogenated under CoFe alloy catalysis to produce  $\text{C}_{2-4}$  hydrocarbons *via* the FTS process. Zhang's team<sup>136</sup> reported a new composite catalyst, InZrO<sub>x</sub>-Beta, showing high selectivity in hydrogenating  $\text{CO}_2$  to butane-enriched  $\text{C}_4$  alkanes. Depositing  $\text{SiO}_2$  on the surface of InZrO<sub>x</sub> effectively inhibited metallic In migration, preventing rapid deactivation of the zeolite part (Fig. 19d). Under photothermal conditions of  $315\text{ }^\circ\text{C}$  and  $3.0\text{ MPa}$ , the InZrO<sub>x</sub>-Beta composite catalyst achieved a butane selectivity of 53.4%, a  $\text{CO}_2$  conversion rate of 20.4%, and a  $\text{CH}_4$  selectivity of about 2% (Fig. 19e). Through the above analysis, the design of two-component catalysts offers a promising strategy to enhance both the activity and selectivity for the production of  $\text{C}_{4+}$  hydrocarbons. By combining complementary active sites, these catalysts facilitate complex reaction pathways, such as C–C coupling and hydrogenation, enabling more efficient synthesis of higher-order hydrocarbons.

Zhang and co-workers<sup>137</sup> reported an iron nitride ( $\text{Fe}_2\text{N}$ ) encapsulated in carbon nanoparticles ( $\text{Fe}_2\text{N}@\text{C}$ ) (Fig. 20a), which showed excellent performance in selectively hydrogenating  $\text{CO}_2$  to  $\text{C}_{2+}$  hydrocarbons. By encapsulating the catalyst with a carbon shell,  $\text{Fe}_2\text{N}@\text{C}$  exhibited outstanding durability, achieving a  $\text{C}_{5+}$  selectivity of 7.52% under pressurized conditions of  $1\text{ MPa}$  (Fig. 20b), enhancing stability and long-term application potential. Zeng *et al.*<sup>138</sup> activated the  $\text{CuFeO}_2$  catalyst under atmospheric pressure to convert  $\text{CO}_2$  and hydrogen ( $\text{H}_2$ ) into long-chain olefins ( $\text{C}_{4+}=\text{}$ ). Under these conditions, the

activated  $\text{CuFeO}_2$  catalyst showed a  $\text{CO}_2$  conversion rate of 27.3% and a  $\text{C}_{4+}=\text{}$  selectivity of 66.9%. In a 50 hours stability test, the  $\text{CO}_2$  conversion rate remained stable, but the  $\text{C}_{4+}=\text{}$  selectivity decreased to 57.6% (Fig. 20c). At a pressure of 30 bar, the  $\text{C}_{4+}=\text{}$  selectivity improved to 66.3%. The experimental results showed that the catalyst's performance could be effectively controlled, and regeneration could be achieved when the catalyst deactivates by adjusting the reaction pressure. In atmospheric pressure  $\text{CO}_2$  hydrogenation, the  $\text{CuFeO}_2$  catalyst remained stable, though its selectivity decreased over time. Increasing the pressure restored catalyst performance, which is significant for industrial applications and catalyst design. Recently, we reported a Cu-promoted CoFe alloy catalyst, which still produced  $\text{C}_{5+}$  products under atmospheric pressure, though the  $\text{C}_{5+}$  selectivity was only 5.7%. The natural light-driven  $\text{CO}_2$  hydrogenation reaction showed excellent activity and selectivity at a weak solar irradiance intensity of  $0.45\text{ kW m}^{-2}$  (0.45 suns) (Fig. 20d).<sup>56</sup>

These findings suggest promising directions for future research aimed at enhancing  $\text{C}_{5+}$  selectivity. Key strategies could include optimizing the metal composition and electronic structure of the active sites, as well as refining catalyst–support interactions to stabilize intermediate species during chain propagation. Additionally, tailoring reaction conditions, such as pressure and temperature, in conjunction with advanced photothermal reactor designs, may further improve catalytic performance.



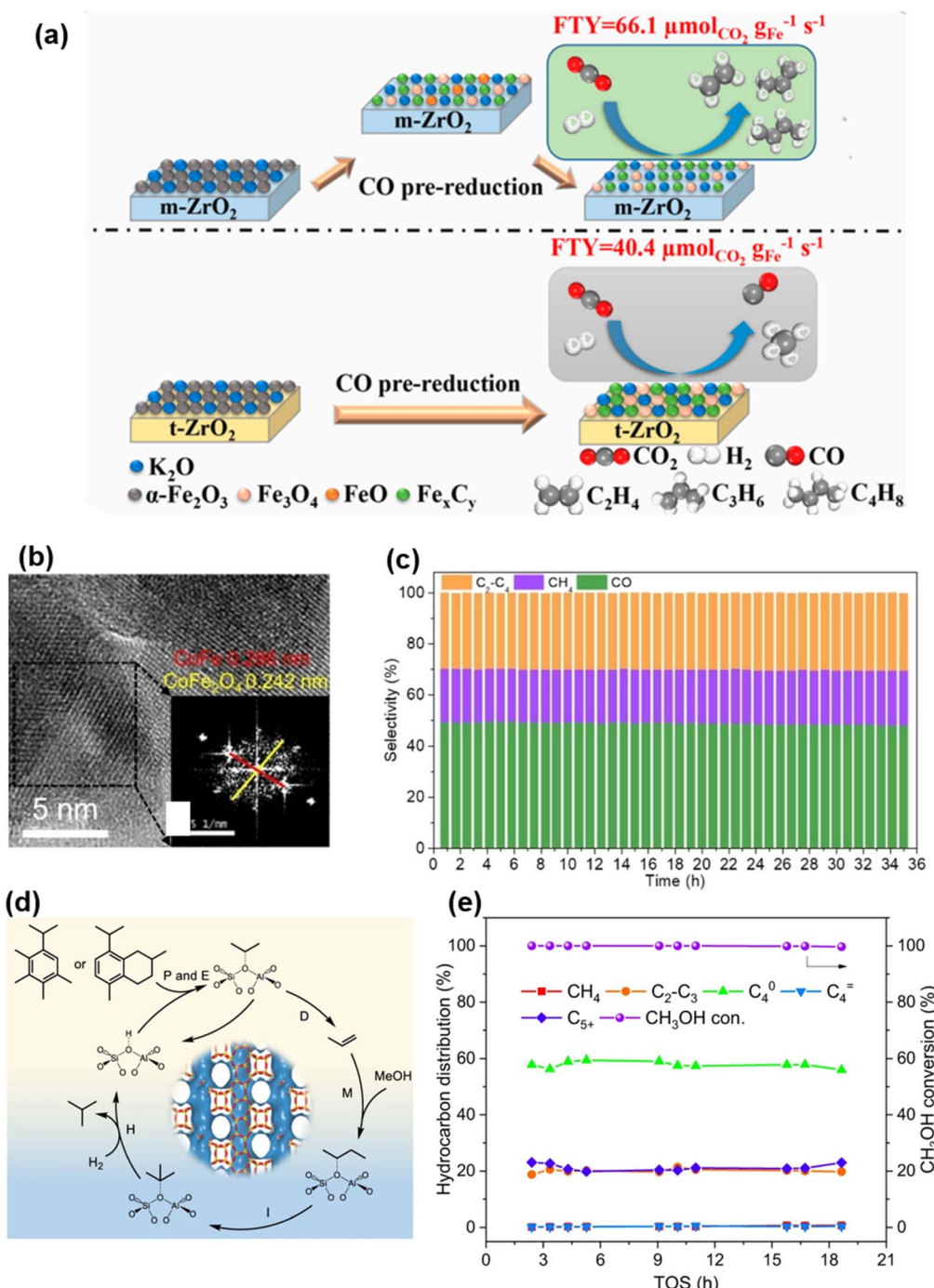


**Fig. 19** (a) Relationship between the physicochemical properties of different types of  $\text{ZrO}_2$  supports and the structure and activity of  $\text{Fe}-\text{K}/\text{ZrO}_2$  catalysts.<sup>135</sup> Copyright 2021, AMER CHEMICAL SOC. (b) HRTEM image of spent  $\text{CoFe}_2\text{O}_4$  (inset image is FFT pattern). (c) Stability of  $\text{CoFe}_2\text{O}_4$  over 35 hours showing the solar-powered hydrogenation of  $\text{CO}_2$  production rate and selectivity towards  $\text{CO}$ ,  $\text{CH}_4$ , and  $\text{C}_{2-4}$ , respectively.<sup>129</sup> Copyright 2023, Wiley. (d) Reaction scheme of butane formation via the side-chain route of aromatic-based cycle. (e)  $\text{CH}_3\text{OH}$  conversion and product distribution for MTH in  $\text{H}_2$  atmosphere over H-Beta.<sup>136</sup> Copyright 2023, Springer Nature.

Looking forward, the integration of such catalysts with renewable energy sources, particularly under solar-driven conditions, holds significant potential for sustainable carbon utilization. The development of robust, scalable systems for selective  $\text{C}_{5+}$  hydrocarbon production could pave the way for new

advancements in solar-to-chemical energy conversion and contribute to achieving carbon-neutral chemical manufacturing.

### 3.4 Ethanol, acetic acid and other products

Photothermal catalysis for the conversion of  $\text{CO}_2$  into high-value-added chemicals, such as fuels, is extremely promising

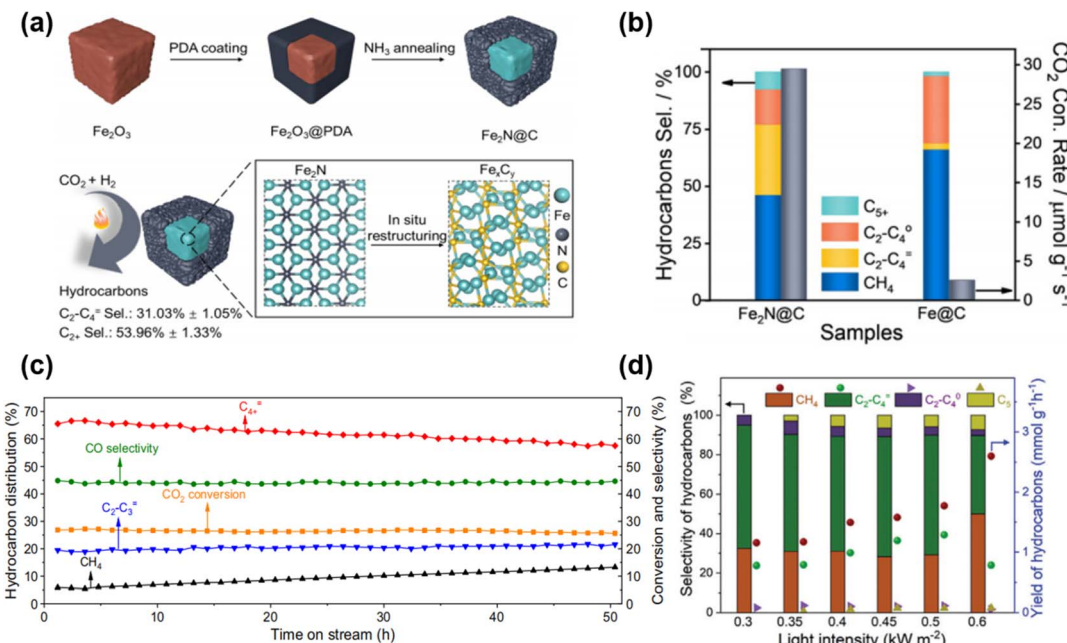


Fig. 20 (a) Synthetic process of Fe<sub>2</sub>N@C nanoparticles and the *in situ* restructuring transformation of Fe<sub>2</sub>N@C into iron carbides during the selective hydrogenation of CO<sub>2</sub> to C<sub>2+</sub> hydrocarbons. (b) CO<sub>2</sub> conversion rate and hydrocarbons selectivity over Fe<sub>2</sub>N@C and Fe@C.<sup>137</sup> Copyright 2021, Wiley. (c) Stability test of activated CuFeO<sub>2</sub>.<sup>138</sup> Copyright 2022, Springer Nature. (d) The CO<sub>2</sub> hydrogenation performance of sunlightdriven Cu<sub>0.65</sub>Co<sub>0.35</sub>Fe<sub>2</sub> catalyst.<sup>56</sup> Copyright 2024, Wiley-VCH Verlag.

as it provides a valuable source of these chemicals while also helping to reduce CO<sub>2</sub> emissions that affect the global climate.<sup>139</sup> This process involves the coupling of photoelectrons produced by the photocatalyst and the dissolution of CO<sub>2</sub> in a water medium, enabling the catalytic conversion of CO<sub>2</sub> into liquid fuels such as ethanol and acetic acid.<sup>140</sup>

Sira Srinives *et al.*<sup>141</sup> utilized a one-step hydrothermal process for the synthesis of precious metal-doped TiO<sub>2</sub>/GO composites. Cu-TiO<sub>2</sub>/GO showed the best photocatalytic performance, which could be attributed to remarkable key parameters, including a high specific surface area, a narrowed band gap energy, and a big crystallite size (Fig. 21a).

Acetic acid is a valuable chemical suitable for industrial intermediates and fuel additives. Zhang *et al.*<sup>142</sup> reported the controllable preparation of highly ordered mesoporous cobalt oxides with modulated surface states to achieve efficient photothermal water-steam reforming of CO<sub>2</sub> to C<sub>2</sub> products with high activity and tunable selectivity (Fig. 21b and c). Pristine mesoporous Co<sub>3</sub>O<sub>4</sub> exhibited an acetic acid selectivity of 96% with a yield rate of 73.44 μmol g<sup>-1</sup> h<sup>-1</sup>.

Acetaldehyde (CH<sub>3</sub>CHO) is an indispensable intermediate in the production of high value-added chemicals, and is widely used in medicine, pesticides and spices.<sup>144</sup> Photocatalytic conversion of CO<sub>2</sub> to acetaldehyde has become a promising method for sustainable production of acetaldehyde. Wang *et al.*<sup>143</sup> Reported the selective photocatalytic hydrogenation of CO<sub>2</sub> to CH<sub>3</sub>CHO using a modified polymeric carbon nitride (PCN) under mild conditions (Fig. 21d). The locally crystallized PCN offers a photocatalytic activity of 1814.7 μmol h<sup>-1</sup> g<sup>-1</sup> with a high selectivity of 98.3% for CH<sub>3</sub>CHO production and

a quantum efficiency of 22.4% at 385 nm, outperforming all the state-of-art CO<sub>2</sub> photocatalysts. The promoted formation of the \*OCCHO intermediate on the locally crystallized PCN is disclosed as the key factor leading to the highly selective CH<sub>3</sub>CHO generation.

### 3.5 Dimethyl carbonate, ethyl-carbonate and other carbonates

Compared to CO<sub>2</sub> reduction into C<sub>1</sub> chemicals like CH<sub>3</sub>OH or formate, non-redox CO<sub>2</sub> chemical fixation offers a route to high-value long-chain products. DMC, with its methoxy and carbonyl groups, can replace toxic phosgene and dimethyl sulfate in methylation and carbonylation reactions and serves as an important electrolyte solvent for lithium-ion batteries due to its high dielectric constant.<sup>145-153</sup> Thus, direct synthesis of DMC from CO<sub>2</sub> has significant theoretical and practical value. Chen *et al.* reported light-driven CO<sub>2</sub> activation into DMC over B<sub>2</sub>O<sub>3</sub> atomic layers with oxygen vacancies, achieving nearly 100% selectivity under mild conditions.<sup>154</sup> These vacancies provided unsaturated sites, enhancing CO<sub>2</sub> and CH<sub>3</sub>OH adsorption. Xie *et al.*<sup>155</sup> found that frustrated Lewis pairs (FLP) sites on CeO<sub>2</sub> with rich FLP sites improved reaction activity, achieving a high yield of DMC up to 15.3 mmol g<sup>-1</sup> (Fig. 22a and b). They used density functional theory to investigate the reaction mechanism on the FLP site, providing insights into CO<sub>2</sub> chemical conversion to long-chain chemicals. They proposed an in-plane heterostructure strategy to construct Lewis acid-base sites for efficient CO<sub>2</sub> activation. Using ultrathin in-plane Cu<sub>2</sub>O/Cu heterostructures as a prototype, they showed that Lewis acid-base sites on the heterointerface facilitate mixed C and O dual



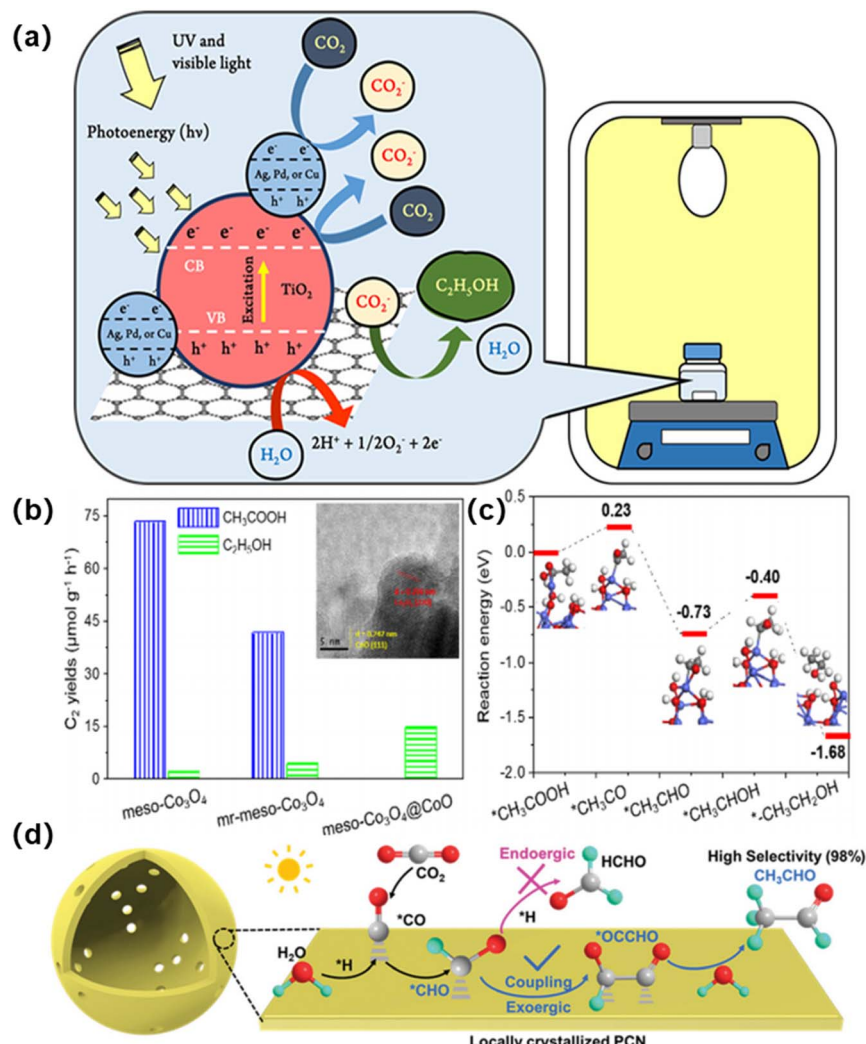


Fig. 21 (a) Schematic diagram exhibiting proposed reaction mechanisms for the photoreduction of  $\text{CO}_2$  on  $\text{Ag}-\text{TiO}_2/\text{GO}$ ,  $\text{Pd}-\text{TiO}_2/\text{GO}$ , and  $\text{Cu}-\text{TiO}_2/\text{GO}$ .<sup>141</sup> Copyright 2021, Royal Society of Chemistry. (b)  $\text{C}_2$  product yield rates, evolutions over time and catalytic stabilities of pristine meso- $\text{Co}_3\text{O}_4$ , mr-meso- $\text{Co}_3\text{O}_4$ , and meso- $\text{Co}_3\text{O}_4@\text{CoO}$ . (c) Pathway on surface-reduced meso- $\text{Co}_3\text{O}_4$ .<sup>142</sup> Copyright 2023, American Chemical Society. (d) The proposed reaction mechanism for the photocatalytic  $\text{CO}_2$  reduction conversion to  $\text{CH}_3\text{CHO}$ .<sup>143</sup> Copyright 2022, Royal Society of Chemistry.

coordination on the surface, strengthening  $\text{CO}_2$  adsorption and activation. DRIFTS revealed that these sites could activate  $\text{CO}_2$  to  $\text{CO}_2^-$  species, a key intermediate for  $\text{CO}_2$  fixation (Fig. 22c–f).

Despite significant progress in  $\text{CO}_2$  chemical fixation to DMC, major challenges and opportunities remain.<sup>157</sup> The overall performance of DMC generation from  $\text{CO}_2$  still falls short of practical application requirements, necessitating the development of advanced catalysts. Therefore, exploring and constructing new catalyst systems with high efficiency for activating  $\text{CO}_2$  into DMC is crucial and presents many future opportunities.

The carbonylation of ethanol using  $\text{CO}_2$  as a carbonyl source to synthesize value-added esters holds significant potential but remains a considerable challenge due to the difficulty of activating inert  $\text{CO}_2$ .<sup>158</sup> Harsh reaction conditions often lead to undesired side reactions, including the activation of the  $\alpha$ -C–H bond and even cleavage of the C–C bond in ethanol, which

hinders the selective activation of the O–H bond.<sup>159</sup> To address these challenges, we propose a photo-thermal cooperative strategy for the carbonylation of ethanol with  $\text{CO}_2$ . This approach utilizes photo-catalysis to activate  $\text{CO}_2$  into reactive  $\text{CO}$ , assisted by  $^*\text{H}$  generated from the thermally-catalyzed dissociation of the alcoholic O–H bond.

To realize this strategy, a  $\text{Cu}_2\text{O}-\text{SrTiCuO}_{3-x}$  catalyst has been designed, featuring abundant interfacial sites and oxygen vacancies to facilitate the reaction (Fig. 22g and h).<sup>156</sup> Under photo-thermal conditions ( $3.29 \text{ W cm}^{-2}$  UV/Visible light irradiation,  $144^\circ\text{C}$ , and  $0.2 \text{ MPa}$   $\text{CO}_2$ ), the catalyst achieved an ethyl formate production rate of  $320 \mu\text{mol g}^{-1} \text{h}^{-1}$  with an impressive selectivity of 85.6% toward the targeted activation of the alcoholic O–H bond. This work demonstrates the potential of leveraging photo-thermal synergy and tailored catalytic materials for efficient  $\text{CO}_2$  utilization and selective carbonates production under mild conditions.

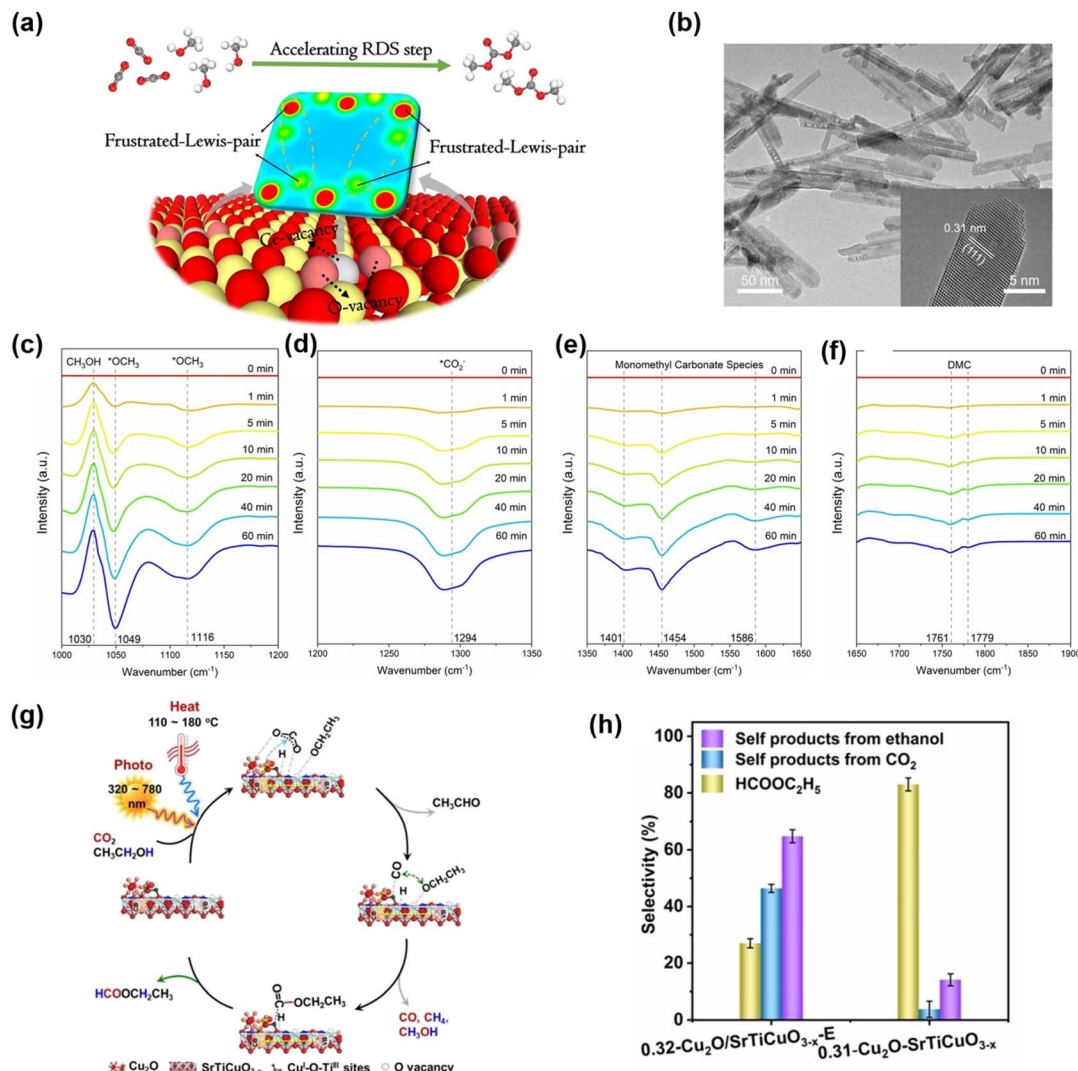


Fig. 22 (a) Illustration of reaction route for the direct DMC synthesis from CO<sub>2</sub> and CH<sub>3</sub>OH on CeO<sub>2</sub>. (b) TEM image of P-CeO<sub>2</sub>-NR, where the inset is corresponding HRTEM image. (c–f) *In situ* DRIFTS for the direct DMC synthesis from CO<sub>2</sub> and CH<sub>3</sub>OH under simulated experimental condition. <sup>155</sup> Copyright 2022, Wiley. (g) Illustrations of reaction mechanism for the carbonylation of ethanol with CO<sub>2</sub> on Cu<sub>2</sub>O-SrTiCuO<sub>3-x</sub> under UV/Visible light irradiation. (h) CO<sub>2</sub> activation rate and formation rate of self-products from CO<sub>2</sub>. <sup>156</sup> Copyright 2023, Wiley.

## 4. Conclusions and outlooks

Solar-driven catalytic conversion of CO<sub>2</sub> into value-added C<sub>2+</sub> chemicals/fuels has been a focus of research in the past decades due to its significance in the energy and environment fields. However, due to the slow reduction kinetics, the photocatalytic reduction of CO<sub>2</sub> remains challenging. The state-of-the-art photocatalytic systems in such route suffer from low efficiency, which is still far from practical application. Therefore, it is of great interest to explore alternate catalytic reaction routes driven by solar energy for efficient CO<sub>2</sub> reduction. Recent pioneering work by several groups, including ours, has shown that photocatalysis coupling of photothermal catalysis for CO<sub>2</sub> reduction is a novel and promising strategy for CO<sub>2</sub> catalytic conversion into C<sub>2+</sub> products.

This review has explored the current state of light-driven CO<sub>2</sub> reduction, tracing its historical development, elucidating the

underlying mechanisms, and examining the pivotal advancements in catalyst design and emphasizing its potential for converting CO<sub>2</sub> into valuable C<sub>2+</sub> products. Historically, photothermal CO<sub>2</sub> reduction has progressed from basic studies to more advanced applications, utilizing the combined effects of light absorption and heat to drive catalytic reaction. Integrating photothermal effects with photocatalysis has significantly improved the efficiency and selectivity of CO<sub>2</sub> reduction, especially for producing C<sub>2+</sub> hydrocarbons. Understanding the mechanisms of photothermal CO<sub>2</sub> conversion has revealed pathways for creating C<sub>2+</sub> products, highlighting the crucial role of simultaneously activating CO<sub>2</sub> and hydrogen sources under solar light.

Catalyst design is critical for advancing solar-driven synthesis of C<sub>2+</sub> products. Surface defect engineering has proven effective in enhancing catalyst performance by creating active sites that improve CO<sub>2</sub> adsorption and activation.



Additionally, designing bifunctional active sites facilitates multi-electron transfer processes, boosting the production of long-chain hydrocarbons. These advancements in catalyst design are essential for addressing the challenges of selectively producing  $C_{2+}$  products.

Solar-driven  $CO_2$  reduction involves various pathways, from producing  $C_1$  products like  $CO$ ,  $CH_4$  and  $CH_3OH$  to high value-added  $C_{2-4}$  hydrocarbons. Photothermal catalysis shows great promise in increasing the efficiency of these reactions by providing the necessary heat to drive endothermic steps and stabilize intermediates. However, producing  $C_{5+}$  hydrocarbons remains challenging due to the complexity of the reaction mechanisms and the need for highly selective and stable catalysts.

Looking ahead, producing  $C_{5+}$  products is a promising but challenging goal that requires innovative catalyst designs and reaction engineering. Future research should focus on developing bifunctional catalysts with highly selective active sites to enable the formation of longer-chain hydrocarbons while minimizing side reactions. Develop reactor systems that maximize light absorption and distribution within the catalytic environment, ensuring efficient utilization of photonic energy for optimizing the intermediates selective coupling and accelerating the reaction rate of  $CO_2$  hydrogenation. Our group has developed advanced photothermal reactor devices that harness natural outdoor sunlight for  $CO_2$  conversion, producing valuable products such as  $CO$ ,  $CH_4$ , and multi-hydrocarbons.<sup>8,56</sup> These systems offer a scalable, sustainable solution for efficient  $CO_2$  hydrogenation, providing a promising path for carbon capture and utilization. Additionally, integrating computational modeling and *in situ* characterization techniques will be crucial for understanding the detailed reaction pathways and optimizing conditions for  $C_{5+}$  synthesis.

The advancement of light-driven photothermal  $CO_2$  reduction goes beyond environmental benefits, providing a sustainable route for chemical synthesis and energy storage. Overcoming current limitations will enable scalable and economically viable  $CO_2$  conversion technologies. Producing higher-order hydrocarbons like ethanol, acetic acid, and various carbonates can significantly impact the chemical industry by offering renewable alternatives to fossil-based materials.

In summary, significant progress has been made in photothermal  $CO_2$  reduction, but developing effective strategies for synthesizing  $C_{2+}$  products remains an exciting challenge. Continued interdisciplinary efforts, combining advances in materials science, catalysis, and reaction engineering, are essential to fully utilize solar energy for the sustainable and selective conversion of  $CO_2$  into a wide range of valuable chemicals. The future of this field is promising, with the potential to greatly contribute to environmental sustainability and the growth of green chemistry.

## Data availability

Data availability is not applicable to this review article as no new data were created or analyzed in this study.

## Author contributions

All of the authors contributed to the manuscript preparation. S. N. and J. Y. conceived the outline of the manuscript. X. W., S. Z., S. N., C. Y., L. L., L. T., R. L., X. Y., Y. Z., S. C. wrote the original draft of the manuscript. X. W., S. Z., S. N., J. W. and J. Y. discussed and helped revise the manuscript.

## Conflicts of interest

There are no conflicts to declare.

## Acknowledgements

This work was supported by the National Natural Science Foundation of China (Grant No. 22402046, U23A20139), the Hebei Natural Science Foundation (Grant nos. B2023201020, B2024201096, 2023HBQZYCXY001, E2023201019), the Hebei Education Department Foundation (Grant No. QN2025190, CXZX2025016), the China Postdoctoral Science Foundation (Grant No. 2023M743770), Industry-University-Research Cooperation Major Projects of Shijiazhuang City (241130477A) and Hebei Province Innovation Capability Enhancement Plan Project (22567620H).

## References

- 1 S. Yang, D. Yang, W. Shi, C. Deng, C. Chen and S. Feng, *Environ. Sci. Pollut. Res.*, 2023, **30**, 81725–81744.
- 2 Z. Xiao, P. Li, H. Zhang, S. Zhang, Y. Zhao, J. Gu, Z. Lian, G. Li, J. J. Zou and D. Wang, *J. Colloid Interface Sci.*, 2024, **672**, 642–653.
- 3 P. Zhang, X. Sui, Y. Wang, Z. Wang, J. Zhao, Y. Weng and J. Long, *J. Am. Chem. Soc.*, 2023, **145**, 5769–5777.
- 4 Z. Lu, Y. F. Xu, Z. S. Zhang, J. C. Sun, X. Ding, W. Sun, W. G. Tu, Y. Zhou, Y. F. Yao, G. A. Ozin, L. Wang and Z. G. Zou, *J. Am. Chem. Soc.*, 2023, **145**, 26052–26060.
- 5 C. Qiu, J. Sun, M. Li, C. Mao, R. Song, Z. Zhang and L. Wang, *J. Am. Chem. Soc.*, 2024, **146**, 33997–34007.
- 6 Y. J. Li, H. M. Liu, L. Ma, J. X. Liu and D. H. He, *Acta Phys.-Chim. Sin.*, 2024, **40**, 2308005.
- 7 H. H. Ou, S. B. Ning, P. Zhu, S. H. Chen, A. Han, Q. Kang, Z. F. Hu, J. H. Ye, D. S. Wang and Y. D. Li, *Angew. Chem., Int. Ed.*, 2022, **61**, e202206579.
- 8 C. Lv, X. Bai, S. Ning, C. X. Song, Q. Guan, B. Liu, Y. Li and J. Ye, *ACS Nano*, 2023, **17**, 1725–1738.
- 9 S. Ning, H. Ou, Y. Li, C. Lv, S. Wang, D. Wang and J. Ye, *Angew. Chem., Int. Ed.*, 2023, **62**, e202302253.
- 10 J. Q. Zhao, R. Shi, G. I. N. Waterhouse and T. R. Zhang, *Nano Energy*, 2022, **102**, 107650.
- 11 G. Y. Chen, H. Ågren, T. Y. Ohulchanskyy and P. N. Prasad, *Chem. Soc. Rev.*, 2015, **44**, 1680–1713.
- 12 L. Yuan, M. Y. Qi, Z. R. Tang and Y. J. Xu, *Angew. Chem., Int. Ed.*, 2021, **60**, 21150–21172.
- 13 Y. Qi, L. Song, S. Ouyang, X. Liang, S. Ning, Q. Zhang and J. Ye, *Adv. Mater.*, 2020, **32**, 1903915.



14 J. Xie, Y. H. Jiang, S. Y. Li, P. Xu, Q. Zheng, X. Y. Fan, H. L. Peng and Z. Y. Tang, *Acta Phys.-Chim. Sin.*, 2023, **39**, 2306037.

15 L. K. Zhao, Y. H. Qi, L. Z. Song, S. B. Ning, S. X. Ouyang, H. Xu and J. H. Ye, *Angew. Chem., Int. Ed.*, 2019, **58**, 7708–7712.

16 G. G. Liu, T. Wang, H. B. Zhang, X. G. Meng, D. Hao, K. Chang, P. Li, T. Kako and J. H. Ye, *Angew. Chem., Int. Ed.*, 2015, **54**, 13561–13565.

17 J. J. Wang, S. Kattel, C. J. Hawhurst, J. H. Lee, B. M. Tackett, K. Chang, N. Rui, C. J. Liu and J. G. G. Chen, *Angew. Chem., Int. Ed.*, 2019, **58**, 6271–6275.

18 H. Song, X. G. Meng, Z. J. Wang, H. M. Liu and J. H. Ye, *Joule*, 2019, **3**, 1606–1636.

19 F. Jiao, J. J. Li, X. L. Pan, J. P. Xiao, H. B. Li, H. Ma, M. M. Wei, Y. Pan, Z. Y. Zhou, M. R. Li, S. Miao, J. Li, Y. F. Zhu, D. Xiao, T. He, J. H. Yang, F. Qi, Q. Fu and X. H. Bao, *Science*, 2016, **351**, 1065–1068.

20 H. B. Zhang, J. Wei, J. C. Dong, G. G. Liu, L. Shi, P. F. An, G. X. Zhao, J. T. Kong, X. J. Wang, X. G. Meng, J. Zhang and J. H. Ye, *Angew. Chem., Int. Ed.*, 2016, **55**, 14308–14312.

21 Q. Kang, T. Wang, P. Li, L. Liu, K. Chang, M. Li and J. Ye, *Angew. Chem., Int. Ed.*, 2015, **54**, 841–845.

22 E. Pipelzadeh, V. Rudolph, G. Hanson, C. Noble and L. Z. Wang, *Appl. Catal., B*, 2017, **218**, 672–678.

23 P. Zhang, J. Li, H. Huang, X. Sui, H. Zeng, H. Lu, Y. Wang, Y. Jia and J. Long, *J. Am. Chem. Soc.*, 2024, **146**, 24150–24157.

24 C. Chen, D. Liu, Y. J. Wu, W. B. Bi, X. K. Sun, X. Chen, W. Liu, L. Xu, H. W. Song and Q. L. Dai, *Nano Energy*, 2018, **53**, 849–862.

25 P. Sabatier, *Comptes Rendus*, 1902, **134**, 514–516.

26 A. Fujishima and K. Honda, *Nature*, 1972, **238**, 37–38.

27 Q. Zhang, A. Mirzaei, Y. Wang, G. Song, C. Wang, L. V. Besteiro, A. O. Govorov, M. Chaker and D. Ma, *Appl. Catal., B*, 2022, **317**, 121792.

28 S. Zhu and D. Wang, *Adv. Energy Mater.*, 2017, **7**, 1700841.

29 L. Buzzetti, G. E. Crisenza and P. Melchiorre, *Angew. Chem., Int. Ed.*, 2019, **58**, 3730–3747.

30 M. Sayed, J. Yu, G. Liu and M. Jaroniec, *Chem. Rev.*, 2022, **122**, 10484–10537.

31 Z. Wei, W. Wang, W. Li, X. Bai, J. Zhao, E. C. Tse, D. L. Phillips and Y. Zhu, *Angew. Chem., Int. Ed.*, 2021, **60**, 8236–8242.

32 Q. Zhang, S. Huang, J. Deng, D. T. Gangadharan, F. Yang, Z. Xu, G. Giorgi, M. Palummo, M. Chaker and D. Ma, *Adv. Funct. Mater.*, 2019, **29**, 1902486.

33 Y. Zhao, S. Zhang, R. Shi, G. I. Waterhouse, J. Tang and T. Zhang, *Mater. Today*, 2020, **34**, 78–91.

34 J. Hao, B. Li, X. Li, X. Zeng, S. Zhang, F. Yang, S. Liu, D. Li, C. Wu and Z. Guo, *Adv. Mater.*, 2020, **32**, 2003021.

35 Q. Zhang, F. Yang, Z. Xu, M. Chaker and D. Ma, *Nanoscale Horiz.*, 2019, **4**, 579–591.

36 B. Zhou, B. Shi, D. Jin and X. Liu, *Nat. Nanotechnol.*, 2015, **10**, 924–936.

37 M. Grätzel, *Nature*, 2001, **414**, 338–344.

38 J. Kizlink, *Collect. Czech. Chem. Commun.*, 1993, **58**, 1399–1402.

39 J. R. Rostrup-Nielsen, *Catal. Sci. Technol.*, 1984, **5**, 1–117.

40 M. Anpo and M. Takeuchi, *J. Catal.*, 2003, **216**, 505–516.

41 G. A. Olah, *Angew. Chem., Int. Ed.*, 2013, **52**, 104–107.

42 A. Kumar and G. Pandey, *Mater. Sci. Eng. Int. J.*, 2017, **1**, 1–10.

43 J. Ran, M. Jaroniec and S. Z. Qiao, *Adv. Mater.*, 2018, **30**, 1704649.

44 X. Meng, T. Wang, L. Liu, S. Ouyang, P. Li, H. Hu, T. Kako, H. Iwai, A. Tanaka and J. Ye, *Angew. Chem., Int. Ed.*, 2014, **53**, 11478–11482.

45 Z. Q. Wang, Z. Q. Yang, Z. C. Kadirova, M. N. Guo, R. M. Fang, J. He, Y. F. Yan and J. Y. Ran, *Coord. Chem. Rev.*, 2022, **473**, 37.

46 Y. Li, R. Z. Li, Z. H. Li, W. Q. Wei, S. X. Ouyang, H. Yuan and T. R. Zhang, *Chem. Res. Chin. Univ.*, 2020, **36**, 1006–1012.

47 L. L. Zhu, M. M. Gao, C. K. N. Peh and G. W. Ho, *Mater. Horiz.*, 2018, **5**, 323–343.

48 R. Ma, J. Sun, D. H. Li and J. J. Wei, *Int. J. Hydrogen Energy*, 2020, **45**, 30288–30324.

49 S. W. Chen, X. Cao, N. Wang, L. Ma, H. R. Zhu, M. Willander, Y. Jie and Z. L. Wang, *Adv. Energy Mater.*, 2017, **7**, 1601255.

50 W. Zhang, L. Wang, K. Wang, M. U. Khan, M. Wang, H. Li and J. Zeng, *Small*, 2017, **13**, 1602583.

51 Y. He, Q. Lei, C. Li, Y. Han, Z. Shi and S. Feng, *Mater. Today*, 2021, **50**, 358–384.

52 G. Chen, R. Gao, Y. Zhao, Z. Li, G. I. Waterhouse, R. Shi, J. Zhao, M. Zhang, L. Shang, G. Sheng, X. Zhang, X. Wen, L. Wu, C. Tung and T. Zhang, *Adv. Mater.*, 2018, **30**, 1704663.

53 Y. Zhou, Z. Wang, L. Huang, S. Zaman, K. Lei, T. Yue, Z. a. Li, B. You and B. Y. Xia, *Adv. Energy Mater.*, 2021, **11**, 2003159.

54 N. L. Reddy, V. N. Rao, M. Vijayakumar, R. Santhosh, S. Anandan, M. Karthik, M. Shankar, K. R. Reddy, N. P. Shetti and M. Nadagouda, *Int. J. Hydrogen Energy*, 2019, **44**, 10453–10472.

55 S. Ning, Y. Sun, S. Ouyang, Y. Qi and J. Ye, *Appl. Catal., B*, 2022, **310**, 121063.

56 S. Ning, J. Wang, X. Wu, L. Li, S. Zhang, S. Chen, X. Ren, L. Gao, Y. Hao, C. Lv, Y. Li and J. Ye, *Adv. Funct. Mater.*, 2024, **34**, 2400798.

57 M. G. Kibria, J. P. Edwards, C. M. Gabardo, C. T. Dinh, A. Seifitokaldani, D. Sinton and E. H. Sargent, *Adv. Mater.*, 2019, **31**, 1807166.

58 T. Numpilai, C. K. Cheng, J. Limtrakul and T. Witoon, *Process Saf. Environ. Prot.*, 2021, **151**, 401–427.

59 Q. Yang, H. Liu, Y. Lin, D. Su, Y. Tang and L. Chen, *Adv. Mater.*, 2024, **36**, 2310912.

60 X. Ding, W. Liu, J. Zhao, L. Wang and Z. Zou, *Adv. Mater.*, 2025, **37**, 2312093.

61 M. Xu, X. Qin, Y. Xu, M. Wang, X. Liu and D. Ma, *Nat. Commun.*, 2022, **13**, 6720.

62 R. C. Brady III and R. Pettit, *J. Am. Chem. Soc.*, 1981, **103**, 1287–1289.



63 G. K. K. Gunasooriya, A. P. van Bavel, H. P. Kuipers and M. Saeyns, *ACS Catal.*, 2016, **6**, 3660–3664.

64 Z. Li, J. Wang, Y. Qu, H. Liu, C. Tang, S. Miao, Z. Feng, H. An and C. Li, *ACS Catal.*, 2017, **7**, 8544–8548.

65 C. Yang, R. Mu, G. Wang, J. Song, H. Tian, Z.-J. Zhao and J. Gong, *Chem. Sci.*, 2019, **10**, 3161–3167.

66 L. Wang, Y. Yi, C. Wu, H. Guo and X. Tu, *Angew. Chem. Int. Ed.*, 2017, **129**, 13867–13871.

67 B. Liu, C. Li, G. Zhang, X. Yao, S. S. Chuang and Z. Li, *ACS Catal.*, 2018, **8**, 10446–10456.

68 G. Centi and S. Perathoner, *Catal. Today*, 2009, **148**, 191–205.

69 H. Kusama, K. Okabe, K. Sayama and H. Arakawa, *Energy*, 1997, **22**, 343–348.

70 H. Kusama, K. Okabe, K. Sayama and H. Arakawa, *Catal. Today*, 1996, **28**, 261–266.

71 A. W. Budiman, J. S. Nam, J. H. Park, R. I. Mukti, T. S. Chang, J. W. Bae and M. J. Choi, *Catal. Surv. Asia*, 2016, **20**, 173–193.

72 W. Jian-Feng, Y. Si-Min, W. W. David, F. Yan-Xin, B. Shi, Z. Chuan-Wei, G. Qiang, H. Jun and W. Wei, *J. Am. Chem. Soc.*, 2013, **135**, 13567–13573.

73 S. Wang, S. Guo, Y. Luo, Z. Qin, Y. Chen, M. Dong, J. Li, W. Fan and J. Wang, *Catal. Sci. Technol.*, 2019, **9**, 6613–6626.

74 P. Zhang, X. Yang, X. Hou, J. Mi, Z. Yuan, J. Huang and C. Stampfl, *Catal. Sci. Technol.*, 2019, **9**, 6297–6307.

75 Y. Zhao, C. Cui, J. Han, H. Wang, X. Zhu and Q. Ge, *J. Am. Chem. Soc.*, 2016, **138**, 10191–10198.

76 B. D. Montejo-Valencia, Y. J. Pagán-Torres, M. M. Martínez-Iñesta and M. C. Curet-Arana, *ACS Catal.*, 2017, **7**, 6719–6728.

77 P. Tundo and M. Selva, *Acc. Chem. Res.*, 2002, **35**, 706–716.

78 S. Fang and K. Fujimoto, *Appl. Catal., A*, 1996, **142**, L1–L3.

79 K. Xie, N. Umezawa, N. Zhang, P. Reunchan, Y. Zhang and J. Ye, *Energy Environ. Sci.*, 2011, **4**, 4211–4219.

80 G. Xi, S. Ouyang, P. Li, J. Ye, Q. Ma and N. Su, *Angew. Chem., Int. Ed.*, 2012, **51**, 2395–2399.

81 H. Pang, X. Meng, P. Li, K. Chang, W. Zhou, X. Wang, X. Zhang, W. Jevasuwan, N. Fukata, D. Wang and J. Ye, *ACS Energy Lett.*, 2019, **4**, 1387–1393.

82 S. Sorcar, J. Thompson, Y. Hwang, Y. H. Park, T. Majima, C. A. Grimes, J. R. Durrant and S.-I. In, *Energy Environ. Sci.*, 2018, **11**, 3183–3193.

83 X. Chen, L. Liu, P. Y. Yu and S. S. Mao, *Science*, 2011, **331**, 746.

84 S. Sun, M. Watanabe, J. Wu, Q. An and T. Ishihara, *J. Am. Chem. Soc.*, 2018, **140**, 6474–6482.

85 F. Lei, Y. Sun, K. Liu, S. Gao, L. Liang, B. Pan and Y. Xie, *J. Am. Chem. Soc.*, 2014, **136**, 6826–6829.

86 Y. Qi, L. Song, S. Ouyang, X. Liang, S. Ning, Q. Zhang and J. Ye, *Adv. Mater.*, 2020, **32**, 1903915.

87 Y. Sun, S. Gao, F. Lei, J. Liu, L. Liang and Y. Xie, *Chem. Sci.*, 2014, **5**, 3976–3982.

88 Y. Sun, J. Chen, X. Du, J. Cui, X. Chen, C. Wu, X. Yang, L. Liu and J. Ye, *Angew. Chem. Int. Ed.*, 2024, **63**, e202410802.

89 L. Ye, X. Jin, Y. Leng, Y. Su, H. Xie and C. Liu, *J. Power Sources*, 2015, **293**, 409–415.

90 C. Mao, F. Zuo, Y. Hou, X. Bu and P. Feng, *Angew. Chem., Int. Ed.*, 2014, **126**, 10653–10657.

91 W. Fang, M. Xing and J. Zhang, *Appl. Catal., B*, 2014, **160**, 240–246.

92 J. Jiang, L. Zhang, H. Li, W. He and J. J. Yin, *Nanoscale*, 2013, **5**, 10573–10581.

93 R. B. Anderson, *Fischer-Tropsch synthesis*, United Kingdom: N. p., 1984, p. 311.

94 H. Yang, C. Zhang, P. Gao, H. Wang, X. Li, L. Zhong, W. Wei and Y. Sun, *Catal. Sci. Technol.*, 2017, **7**, 4580–4598.

95 Z. Wang, G. Zou, J. H. Park and K. Zhang, *Sci. China Mater.*, 2024, **67**, 397–423.

96 G. Jia, M. Sun, Y. Wang, Y. Shi, L. Zhang, X. Cui, B. Huang and J. C. Yu, *Adv. Funct. Mater.*, 2022, **32**, 2206817.

97 G. Wang, Z. Chen, T. Wang, D. Wang and J. Mao, *Angew. Chem., Int. Ed.*, 2022, **61**, e202210789.

98 M. O. Olagunju, X. Poole, P. Blackwelder, M. P. Thomas, B. S. Guiton, D. Shukla, J. L. Cohn, B. Surnar, S. Dhar and E. M. Zahran, *ACS Appl. Nano Mater.*, 2020, **3**, 4904–4912.

99 S. Cao, Y. Li, B. Zhu, M. Jaroniec and J. Yu, *J. Catal.*, 2017, **349**, 208–217.

100 D. Gao, W. Liu, Y. Xu, P. Wang, J. Fan and H. Yu, *Appl. Catal., B*, 2020, **260**, 118190.

101 X. Li, J. Yu, M. Jaroniec and X. Chen, *Chem. Rev.*, 2019, **119**, 3962–4179.

102 P. Li, L. Liu, W. An, H. Wang, H. Guo, Y. Liang and W. Cui, *Appl. Catal., B*, 2020, **266**, 118618.

103 J. Ji, R. Li, H. Zhang, Y. Duan, Q. Liu, H. Wang and Z. Shen, *Appl. Catal., B*, 2023, **321**, 122020.

104 R. Schlögl, *Chem. Sustain. Energy Mater.*, 2010, **3**, 209–222.

105 N. L. Panwar, S. C. Kaushik and S. Kothari, *Renewable Sustainable Energy Rev.*, 2011, **15**, 1513–1524.

106 S. Chu, Y. Cui and N. Liu, *Nat. Mater.*, 2017, **16**, 16–22.

107 W. Wang, S. Wang, X. Ma and J. Gong, *Chem. Soc. Rev.*, 2011, **40**, 3703–3727.

108 C. Qiu, J. Sun, M. Li, C. Mao, R. Song, Z. Zhang, D. D. Perovic, J. Y. Howe, L. Wang and G. A. Ozin, *J. Am. Chem. Soc.*, 2024, **146**, 33997–34007.

109 M. Zhang, Y. Zhu, J. Yan, J. Xie, T. Yu, M. Peng, J. Zhao, Y. Xu, A. Li, C. Jia, L. He, M. Wang, W. Zhou, R. Wang, H. Jiang, C. Shi, J. Rodriguez and D. Ma, *Angew. Chem., Int. Ed.*, 2024, e202418645.

110 W. Zhang, Y. Chao, W. Zhang, J. Zhou, F. Lv, K. Wang, F. Lin, H. Luo, J. Li and M. Tong, *Adv. Mater.*, 2021, **33**, 2102576.

111 J. Ma, J. Yu, G. Chen, Y. Bai, S. Liu, Y. Hu, M. Al-Mamun, Y. Wang, W. Gong and D. Liu, *Adv. Mater.*, 2023, **35**, 2302537.

112 Q. Wang, Z. Miao, Y. Zhang, T. Yan, L. Meng and X. Wang, *ACS Catal.*, 2022, **12**, 4016–4025.

113 S. B. Ning, H. Xu, Y. H. Qi, L. Z. Song, Q. Q. Zhang, S. X. Ouyang and J. H. Ye, *ACS Catal.*, 2020, **10**, 4726–4736.

114 F. Jiao, J. Li, X. Pan, J. Xiao, H. Li, H. Ma, M. Wei, Y. Pan, Z. Zhou and M. Li, *Science*, 2016, **351**, 1065–1068.

115 L. Zhong, F. Yu, Y. An, Y. Zhao, Y. Sun, Z. Li, T. Lin, Y. Lin, X. Qi and Y. Dai, *Nature*, 2016, **538**, 84–87.



116 Y. Yang, Z. Chai, X. Qin, Z. Zhang, A. Muhetaer, C. Wang, H. Huang, C. Yang, D. Ma and Q. Li, *Angew. Chem., Int. Ed.*, 2022, **61**, e202200567.

117 Y. Tang, Y. Li, W. Bao, W. Yan, J. Zhang, Y. Huang, H. Li, Z. Wang, M. Liu and F. Yu, *Appl. Catal., B*, 2023, **338**, 123054.

118 Y. Tang, Z. Yang, C. Guo, H. Han, Y. Jiang, Z. Wang, J. Liu, L. Wu and F. Wang, *J. Mater. Chem. A*, 2022, **10**, 12157–12167.

119 Y. Li, Z. Liu, Z. Rao, F. Yu, W. Bao, Y. Tang, H. Zhao, J. Zhang, Z. Wang, J. Li, Z. Huang, Y. Zhou, Y. Li and B. Dai, *Appl. Catal., B*, 2022, **319**, 121903.

120 J. Wang, J. Meeprasert, Z. Han, H. Wang, Z. Feng, C. Tang, F. Sha, S. Tang, G. Li and E. A. Pidko, *Chin. J. Catal.*, 2022, **43**, 761–770.

121 D. Tian, Y. Men, S. Liu, J. Wang, Z. Li, K. Qin, T. Shi and W. An, *Colloids Surf. A Physicochem. Eng. Asp.*, 2022, **653**, 129945.

122 Q. Yang, V. A. Kondratenko, S. A. Petrov, D. E. Doronkin, E. Saraci, H. Lund, A. Arinchtein, R. Krahnert, A. S. Skrypnik and A. A. Matvienko, *Angew. Chem., Int. Ed.*, 2022, **61**, e202116517.

123 S. Zhu, N. Li, D. Zhang and T. Yan, *J. CO<sub>2</sub> Util.*, 2022, **64**, 102177.

124 Y. Zhang, W. Li, F. Tian, N. Cai, Q. Guan, D. Zhang, W. Ran, N. Li and T. Yan, *Chem. Eng. J.*, 2023, **477**, 147129.

125 Y. Shen, C. Ren, L. Zheng, X. Xu, R. Long, W. Zhang, Y. Yang, Y. Zhang, Y. Yao, H. Chi, J. Wang, Q. Shen, Y. Xiong, Z. Zou and Y. Zhou, *Nat. Commun.*, 2023, **14**, 1117.

126 Z. Li, J. Liu, R. Shi, G. I. Waterhouse, X. D. Wen and T. Zhang, *Adv. Energy Mater.*, 2021, **11**, 2002783.

127 Y. Shi, Z. Li, Q. Hao, R. Li, Y. Li, L. Guo, S. Ouyang, H. Yuan and T. Zhang, *Adv. Funct. Mater.*, 2024, **34**, 2308670.

128 W. Li, Y. Zhang, Y. Wang, W. Ran, Q. Guan, W. Yi, L. Zhang, D. Zhang, N. Li and T. Yan, *Appl. Catal., B*, 2024, **340**, 123267.

129 R. Song, Z. Li, J. Guo, P. N. Duchesne, C. Qiu, C. Mao, J. Jia, S. Tang, Y. F. Xu, W. Zhou, L. Wang, W. Sun, X. Yan, L. Guo, D. Jing and G. Ozin, *Angew. Chem., Int. Ed.*, 2023, **135**, e202304470.

130 L. Liu, A. V. Puga, J. Cored, P. Concepción, V. Pérez-Dieste, H. García and A. Corma, *Appl. Catal., B*, 2018, **235**, 186–196.

131 A. V. Puga and A. Corma, *Top. Catal.*, 2018, **61**, 1810–1819.

132 M. Tahir and N. A. S. Amin, *Int. J. Hydrogen Energy*, 2017, **42**, 15507–15522.

133 C. Song, Z. Wang, J. Zhao, X. Qin, M. Peng, Z. Gao, M. Xu, Y. Xu, J. Yan and Y. Bi, *Chem Catal.*, 2024, **4**, 100960.

134 W. Li, Y. Zhang, W. Ran, Y. Wang, F. Tian, F. Zhang, M. Xu, D. Zhang, N. Li and T. Yan, *Appl. Catal., B*, 2024, **351**, 123978.

135 J. Huang, S. Jiang, M. Wang, X. Wang, J. Gao and C. Song, *ACS Sustain. Chem. Eng.*, 2021, **9**, 7891–7903.

136 H. Wang, S. Fan, S. Guo, S. Wang, Z. Qin, M. Dong, H. Zhu, W. Fan and J. Wang, *Nat. Commun.*, 2023, **14**, 2627.

137 B. Zhao, M. Sun, F. Chen, Y. Shi, Y. Yu, X. Li and B. Zhang, *Angew. Chem., Int. Ed.*, 2021, **133**, 4546–4550.

138 Z. Li, W. Wu, M. Wang, Y. Wang, X. Ma, L. Luo, Y. Chen, K. Fan, Y. Pan, H. Li and J. Zeng, *Nat. Commun.*, 2022, **13**, 2396.

139 W. Tu, Y. Zhou and Z. Zou, *Adv. Mater.*, 2014, **26**, 4607–4626.

140 F. Almomani, R. Bhosale, M. Khraisheh, A. Kumar and M. Tawalbeh, *Appl. Surf. Sci.*, 2019, **483**, 363–372.

141 N. Lertthanaphol, N. Pienutsa, K. Chusri, T. Sornsuchat, P. Chanthara, P. Seeharaj, P. Kim-Lohsoontorn and S. Srinives, *ACS Omega*, 2021, **6**, 35769–35779.

142 Y. Xiong, W. Zhao, D. Gu, Z. Tie, W. Zhang and Z. Jin, *Nano Lett.*, 2023, **23**, 4876–4884.

143 Q. Liu, H. Cheng, T. Chen, T. W. B. Lo, Z. Xiang and F. Wang, *Energy Environ. Sci.*, 2022, **15**, 225–233.

144 D. J. Anneken, S. Both, R. Christoph, G. Fieg, U. Steinberger and A. Westfechtel, Ullmann's encycl, *Chem. Ind.*, 2006, **14**, 74–116.

145 S. Subramanian, Y. Song, D. Kim and C. T. Yavuz, *ACS Energy Lett.*, 2020, **5**, 1689–1700.

146 P. Kumar, V. C. Srivastava, U. L. Štangar, B. Mušić, I. M. Mishra and Y. Meng, *Catal. Rev.*, 2021, **63**, 363–421.

147 S. Subramanian, J. Oppenheim, D. Kim, T. S. Nguyen, W. M. Silo, B. Kim, W. A. Goddard and C. T. Yavuz, *Chem.*, 2019, **5**, 3232–3242.

148 N. Thonemann and M. Pizzol, *Energy Environ. Sci.*, 2019, **12**, 2253–2263.

149 H. Ohno, M. Ikhlayel, M. Tamura, K. Nakao, K. Suzuki, K. Morita, Y. Kato, K. Tomishige and Y. Fukushima, *Green Chem.*, 2021, **23**, 457–469.

150 M. Liu, M. Konstantinova, L. Negahdar and J. McGregor, *Chem. Eng. Sci.*, 2021, **231**, 116267.

151 M.-Y. Zhou, X.-Q. Ding, J.-F. Ding, L.-P. Hou, P. Shi, J. Xie, B.-Q. Li, J.-Q. Huang, X.-Q. Zhang and Q. Zhang, *Joule*, 2022, **6**, 2122–2137.

152 Z. Chang, Y. Qiao, H. Yang, X. Cao, X. Zhu, P. He and H. Zhou, *Angew. Chem., Int. Ed.*, 2021, **60**, 15572–15581.

153 S. Zhang, G. Yang, S. Liu, X. Li, X. Wang, Z. Wang and L. Chen, *Nano Energy*, 2020, **70**, 104486.

154 S. Chen, H. Wang, Z. Kang, S. Jin, X. Zhang, X. Zheng, Z. Qi, J. Zhu, B. Pan and Y. Xie, *Nat. Commun.*, 2019, **10**, 788.

155 L. Li, W. Liu, R. Chen, S. Shang, X. Zhang, H. Wang, H. Zhang, B. Ye and Y. Xie, *Angew. Chem., Int. Ed.*, 2022, **134**, e202214490.

156 J. Zhang, C. Shang, Z. An, Y. Zhu, H. Song, Z. Chai, X. Shu, L. Zheng and J. He, *Angew. Chem., Int. Ed.*, 2023, **62**, e202312068.

157 G. Hou, Q. Wang, D. Xu, H. Fan, K. Liu, Y. Li, X. K. Gu and M. Ding, *Angew. Chem., Int. Ed.*, 2024, **63**, e202402053.

158 Y. Cao, R. Guo, M. Ma, Z. Huang and Y. Zhou, *Acta Phys.-Chim. Sin.*, 2024, **40**, 2303029.

159 Y. F. Liang, M. Bilal, L. Y. Tang, T. Z. Wang, Y. Q. Guan, Z. Cheng, M. Zhu, J. Wei and N. Jiao, *Chem. Rev.*, 2023, **123**, 12313–12370.

